Flow Control for Enhanced Aileron Effectiveness on a Commercial Aircraft

Arvin Shmilovich[1] and Yoram Yadlin[2]
Boeing Research and Technology, Huntington Beach, CA, 92647, USA

Paul Vijgen[3]
Boeing Commercial Aircraft, Everett, WA, 98204, USA

Rene Woszidlo[4]
Boeing Research and Technology, Hazelwood, MO, 63042, USA

Active flow control was applied to the ailerons of a representative future short/medium-range twin-engine airplane to improve aerodynamic performance during high-lift operations. The study is aimed at reduced drag and enhanced lift over the range of practical angles of attack, including stall. These benefits translate to airplane performance improvements, such as longer range or larger payload. Various flow control techniques were explored using Computational Fluid Dynamics and the aerodynamic performance enhancements were benchmarked against the baseline configuration. The computational analyses are used to quantify aerodynamic benefits, as well as the input required for actuation. The results were used in a system integration study for identifying potential practical implementations, which are described in a companion paper. Combined with the integration analysis, the objective of this project is to identify the most promising flow control candidates that potentially provide material net airplane level enhancements using onboard fluidic sources. The current study indicates that up to 5% net improvement in L/D at takeoff is potentially achievable using active flow control on the aileron, after accounting for factors of system integration.

I. Nomenclature

Parameters

A_{ref}	Wing reference area
A	Area vector
α	Angle of attack
β	Yaw angle
C_D	Airplane drag coefficient
C_L	Airplane lift coefficient
C_{Lmax}	Maximum lift coefficient
C_m	Airplane pitching moment coefficient
C_μ	Total momentum coefficient, $\dot{m}u_j/(0.5\cdot\rho_\infty u_\infty^2 A_{ref})$
C_p	Pressure coefficient
C_q	Mass flow coefficient, $\dot{m}_j/(\rho_\infty u_\infty A_{ref})$
η	Actuator efficiency

[1] Technical Fellow, Boeing Research and Technology, and AIAA Senior Member.
[2] Aerodynamics Engineer, Boeing Research and Technology, and AIAA Senior Member.
[3] Associate Technical Fellow, Boeing Commercial Aircraft, and AIAA Member.
[4] Technical Lead Engineer, Boeing Research and Technology, and AIAA Associate Fellow.

L/D	Lift-to-drag ratio
Δ(L/D)	Percentage delta in lift-to-drag ratio, $100\cdot[(L/D)_{AFC}-(L/D)_{baseline}]/(L/D)_{baseline}$
M	Mach number
$\dot{m}$	Mass flow
P_{0in}	Total pressure at the actuator inlet
$P_{0\infty}$	Freestream total pressure
PR	Total pressure ratio, $P_{0in}/P_{0\infty}$
PT	Normalized total pressure, $P_0/P_{0\infty}$
Re	Reynolds number based on mean aerodynamic chord
ρ	Density
T_{0in}	Total temperature at the actuator inlet
$T_{0\infty}$	Freestream total temperature
TR	Total temperature ratio, $T_{0in}/T_{0\infty}$
U	Velocity vector
u_∞	Freestream velocity
x,y,z	Streamwise, spanwise and vertical coordinates, respectively

Subscripts

in	Actuator inlet
j	Actuation jet
th	Actuator throat
∞	Freestream
0	Stagnation

Abbreviations

1D	One dimensional
3D	Three dimensional
AFC	Active flow control
APU	Auxiliary Power Unit
CD	Convergent-divergent
CFD	Computational Fluid Dynamics
CRM-HL	Common Research Model – High Lift
GD	Gas dynamics
IB, OB	Inboard, outboard
LaRC	Langley Research Center
NASA	National Aeronautics and Space Administration
OML	Outer mold line
RANS	Reynolds-Averaged Navier-Stokes
SA	Spalart-Allmaras turbulence model

II. Introduction

The need for improved aerodynamic efficiency through the application of Active Flow Control (AFC) has motivated a number of studies over the years. Previous studies [1, 2] investigated potential benefits of reducing the cruise drag associated with modern high-lift systems. Although the performance benefits are tantalizing, that specific application dictates significant architectural changes to the aircraft, rendering it likely impractical for implementation in the next 15–20 years. Therefore, an intermediate application that matures and transitions AFC design and system capabilities in preparation for broader aircraft configuration changes is desired. A pathway toward more practical implementations may utilize localized AFC applications with limited architectural impact on the aircraft. The prospective use of localized AFC has become especially relevant after the successful demonstration of a full-scale AFC system in flight under a collaborative project between NASA and the Boeing Company [3]. In view of these findings, this project focuses on a set of applications targeting smaller regions of the airframe, yet are expected to offer meaningful net performance enhancements with manageable system integration.

Localized AFC applications to commercial transports may lead to substantial environmental and economic advantages for airplane operators. In particular, enhanced high-lift performance is one of the key objectives in aircraft design. Considering takeoff as an example, since the lift-to-drag ratio (L/D) is a major determinant of performance,

an increase in L/D allows for larger airplane payload, reduced runway length, and/or longer range, which translates to substantial economic advantages. Such benefits are illustrated by using several trade factors for a long range two-engine transport [4]:

- A 1.5% increase in maximum lift coefficient is equivalent to a 6,600 lbs increase in payload for a fixed approach speed.
- A 1% increase in takeoff L/D is equivalent to a 2,800 lbs increase in payload or a 150 nm increase in range.
- A 0.1 increase in lift coefficient at constant angle of attack is equivalent to reducing the approach attitude by one degree. As a result, the landing gear may be shortened for a savings in airplane weight of 1,400 lbs.

Moreover, the takeoff and climb-out portions of the flight profile often determine the engine rating and thereby the engine core size. Therefore, applications that improve the L/D will enable a reduction in the engine core size, resulting in lower airplane weight. Consequently, this will lead to lower fuel consumption and reduced emissions. It is noted that comparable gains can be realized for a short/medium range airplane similar to the Reference Aircraft considered here.

Motivated by these performance metrics, Boeing has recently initiated exploratory studies of new flow control concepts for high-lift applications using CFD. The new concepts include customary methods for reduced flow separation as well as unconventional approaches that target additional parameters for enhanced aerodynamic performance. This strategy offers a wider range of opportunities, improving the odds of identifying promising candidates for subsequent development. Promising approaches identified by Boeing for further development target different areas of the wing for AFC implementations. In one application, AFC is used to improve aerodynamic performance of ailerons, which are customarily deflected during high-lift operations. This study focuses on the aileron application. AFC can also be used at specific locations on the wing leading edge in conjunction with slats in order to enhance the performance of the high-lift system. The wing leading edge application for AFC was initially investigated by Shmilovich and Yadlin [5] and it is the subject of a companion paper [6].

The overarching objective of this collaborative NASA/Boeing project is to develop a trade study and business case for the localized AFC applications that could be inserted into the technology development pipeline for upcoming commercial aircraft. This paper focuses on the aileron application and it describes the computational simulations phase of the study. A representative configuration is used at the relevant flight conditions (takeoff and landing, sealed and gapped slats, etc.) with relatively modest configuration changes to accommodate AFC implementations (e.g., larger aileron deflections). Various AFC layouts and actuation techniques are considered. By and large, the AFC methods are designed for the least amount of actuation power required for a specific design goal. The predicted aerodynamic data are used to establish airplane performance gains and to facilitate the integration phase of the study, which is described in a companion paper [7].

The entirety of this NASA/Boeing project is captured by four detailed reports [8–11]. The findings of this study provide guidelines for a planned wind tunnel test for the experimental confirmation of the AFC approaches. Reference 11 describes the initial step in developing the aileron AFC implementation on the CRM-HL (Common Research Model - High Lift) to be tested at the NASA LaRC 14ft by 22ft Subsonic Tunnel (14x22). Additionally, the experimental data will be used to further refine the aircraft level integration and performance estimates, with the goal of enabling practical implementations into future airplanes.

III. Reference Aircraft and Computational Approach

This section describes the geometry of the Reference Aircraft, computational strategy, the geometry setup, and the grid system for the Reference Aircraft. Limited validation for the baseline flow without AFC was performed for two relevant geometries using both flight and wind tunnel data. This is a necessary confidence building step before embarking on the exploratory nature of this AFC study.

A. Geometry of Reference Aircraft

The Reference Aircraft was selected for the study of AFC. It represents a future, short/medium-range, twin-engine transonic airplane. The geometry definition, which includes fuselage, wing, Krueger flaps, slats, single-element flaps, nacelle/chine, aileron, etc., was adequate for CFD analysis. Detents of the high-lift elements were also available. Additional information on the structural layout, propulsion system, optional fluidic and power sources, and weights data for performance analysis and sizing, are discussed in the integration study [7].

High-lift geometries for takeoff and landing are considered. The takeoff configuration consists of a system of sealed slats and a Fowler flap system whose elements are deployed to the takeoff settings. At takeoff, the ailerons are symmetrically deflected to a nominal angle. The landing configuration employs a slotted slat system and flaps at

appropriate detents. Customarily, the ailerons are not deflected during landing. The high-lift system includes sealed Krueger flaps in the regions between the fuselage and engine pylons for both the takeoff and landing conditions.

B. Computational Method

The computational tool used for flow control is a modified version of the OVERFLOW code originally developed by NASA [12] and it forms the core process of Boeing's transport aircraft CFD in the context of AFC. OVERFLOW is based on the unsteady Reynolds-averaged Navier-Stokes (RANS) formulation for overset grid systems. The numerical procedure has been modified to simulate flows for a family of flow control techniques [13, 14]. These include constant blowing, pulsed suction/blowing, swiveling jets (sprinkler), fluidic oscillators and traverse actuation. The simulation tool has been generalized for large systems of actuators [2, 15, 16]. In most flow control applications, the computational domain contains the relevant physical region. It consists of the inner regions of the actuators and the external domain, enabling a complete simulation that captures the interplay amongst the actuator jets and the surrounding flow, irrespective of the actuation input. This coupling approach is adequate for any input pressure, whether the actuator flow is subsonic, choked, or intermittently subsonic/supersonic.

In this study, the second-order Roe upwind-differencing scheme is used with the ARC3D diagonalized Beam-Warming scalar pentadiagonal scheme on the right-hand side. The Spalart-Allmaras (SA) turbulence model has proven robust in the context of the highly separated flows and is used for the simulation cases presented here. The time stepping scheme is second-order as demonstrated in the framework of AFC using a system with multiple actuators [15]. The numerical procedure has been extensively validated for numerous applications of AFC [15, 17] through both wind tunnel settings and flight testing [16]. The validation studies include the characterization of flow control devices for the range of practical actuation parameters, as well as the performance of airplanes equipped with large systems of actuators.

C. Geometry Setup and Grid System

A set of geometric simplifications were introduced to the Reference Aircraft in order to allow for quicker computational turnaround without compromising the modeling of the flow control effects. The horizontal tail, the landing gear and the brackets of the leading edge devices, as well as the flap track fairings are excluded from the computational model. Flow-through engines are used in all the simulations presented here. The wing is rigid, and therefore, no aeroelastic effects are accounted for in the simulations. No yaw conditions are considered here, so the simulations are performed on half of the airplane and assuming a vertical plane of symmetry.

The geometry of the surface grids in Fig. 1 shows close views of the aileron and the slat in the takeoff positions. The single-element flap is deflected to 20°. The aileron is deflected to a nominal angle of 7.5° as customarily used on contemporary takeoff procedures. The wing leading edge consists of a sealed Krueger flap inboard of the engine station. Outboard of the engine there are four slat elements, which are in the sealed position. In the majority of the simulations, the slats are treated as a continuous element, unless otherwise noted.

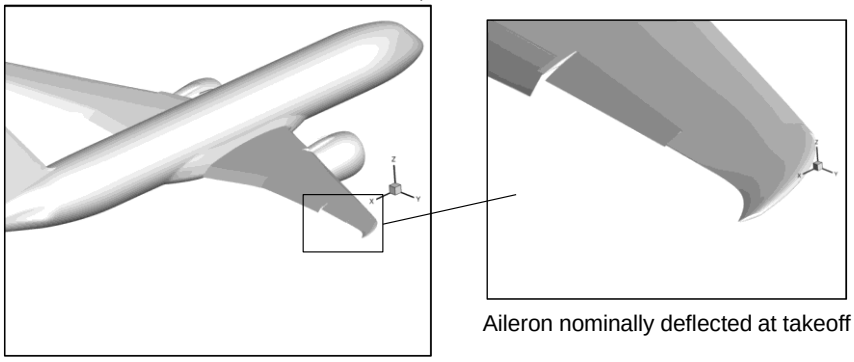

Fig. 1 Takeoff geometry used in the modeling of flow control at the aileron.

D. Code Verification

It is highly desirable to gain confidence in the validity of the computational simulations for AFC using experimental data. However, due to the investigative nature of this study, validation cannot be performed at the present time. Nevertheless, code verification for the baseline flow without AFC was performed for two relevant geometries. The first configuration represents a contemporary short/middle-range airplane. The computational model includes all the relevant high-lift components. Figure 2 shows the CFD geometry and the computed lift compared to measured flight data, indicating good agreement in the range in which data are available.

The second configuration is the Reference Aircraft that will be subsequently used for the AFC study. Here, in lieu of validation, the OVERFLOW solutions were verified with results obtained with another RANS code. CFD++ is a general purpose RANS code that uses a finite volume solver [18]. It is noted that the CFD++ solutions were obtained prior to the current study. Those results were obtained on an unstructured grid system using the SA turbulence model. The OVERFLOW settings were generally aligned with the CFD++ setup.

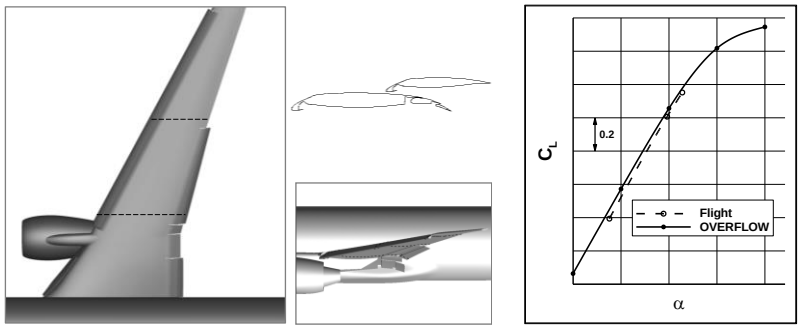

Fig. 2 Validation of OVERFLOW with flight measured data at takeoff conditions.

The OVERFLOW and CFD++ simulations were performed for the takeoff configuration in Fig. 1, which consists of sealed leading edge devices and aileron set at a nominal deflection of 7.5°. A slight difference in the CFD geometries exists as CFD++ includes the flap track fairings whereas OVERFLOW does not. The solutions were obtained in free air and with fully turbulent flow. The freestream Mach number is 0.26 and the Reynolds number based on the mean aerodynamic chord is 6 million. Comparisons of the aerodynamic forces between OVERFLOW and CFD++ are shown in Fig. 3. Generally, there is very good agreement in the linear range of the lift curve even though some differences are noticeable in L/D. Aside from the geometric difference, another factor that might have contributed to this discrepancy is that CFD++ solutions were obtained using low Mach number preconditioning. Based on these code verifications, combined with extensive AFC validation performed previously on numerous AFC applications, the OVERFLOW code is deemed appropriate for evaluation of AFC concepts per the objectives of this study.

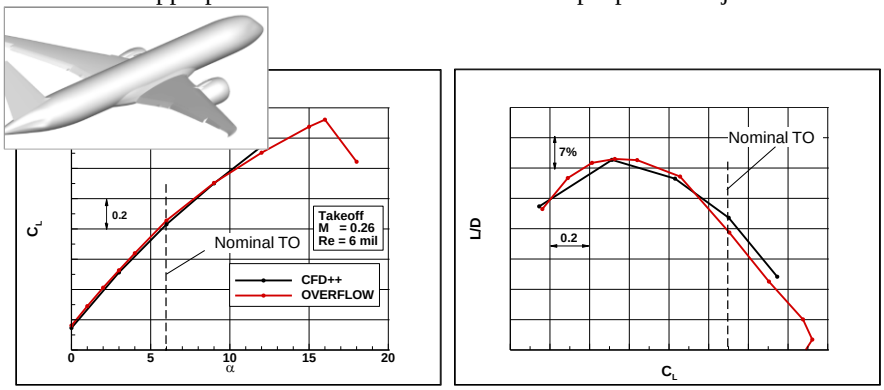

Fig. 3 Comparison of OVERFLOW and CFD++ of the baseline Reference Aircraft at takeoff, M_∞=0.26, Re=6 million.

IV. Results with AFC on Deflected Aileron

Customarily, the ailerons are drooped to a nominal angle to produce high L/D during takeoff. As the aileron is deflected, the increase in wing camber results in added lift. The higher lift leads to an increase in the form and the induced components of drag. Although total airplane drag increases too, a net increase in L/D can be realized if the aileron deflection is sufficiently small. At larger aileron deflections, however, flow separation develops, and the associated drag increase becomes prohibitive, resulting in a drop in L/D. This places a limit on the L/D that can be achieved using drooped ailerons. This constraint can be addressed by improving the flow quality on the aileron. In this application, AFC is used in conjunction with ailerons deflected to higher angles in order to enhance their effectiveness. The following subsections summarize the baseline flow over the aileron, as well as various AFC configurations and parameters over a deflected aileron.

A. Baseline Flow

The first set of results is used to gain insight into the flow development as a function of aileron deflection for the baseline unactuated flow. The aileron is deflected at 0°, 7.5°, 12°, 16° and 25°, where 7.5° is considered the nominal angle for takeoff (also dubbed nominal aileron). The freestream Mach number is 0.20 and Re=6million, consistent with the Reynolds number used in the validation step (Section III.D). The nominal angle of attack at takeoff is 6°.

Figure 4 shows the flow fields for the 0°, 7.5° and 25° aileron deflection angles in terms of the surface pressure distributions, the flow separation bubbles (in either blue or gray for clarity) and the normalized total pressure, PT, at a set of cross-sectional cuts just downstream of the wing. At these conditions, the baseline flow fields contain pockets of flow separation along the trailing edge of the flaps. The flow is fully attached on the undeflected aileron, but progressively larger separation forms at increasingly higher angles, triggered by the adverse pressure gradient close to the hinge line. At the nominal deflection, the flow is separated at the trailing edge of the aileron. However, at the 25° deflection, the entire aileron is separated, indicating a thicker wake with larger total pressure loss. This is indicative of higher drag. The total pressure also indicates that the tip vortex elements get stronger, commensurate with the increased aileron loading at the largest deflection. The tip vortex from the inboard edge of the aileron is particularly coherent. Figure 5 shows the total pressure contours at the midaileron cross-sections, where the black lines denote the regions of flow reversal.

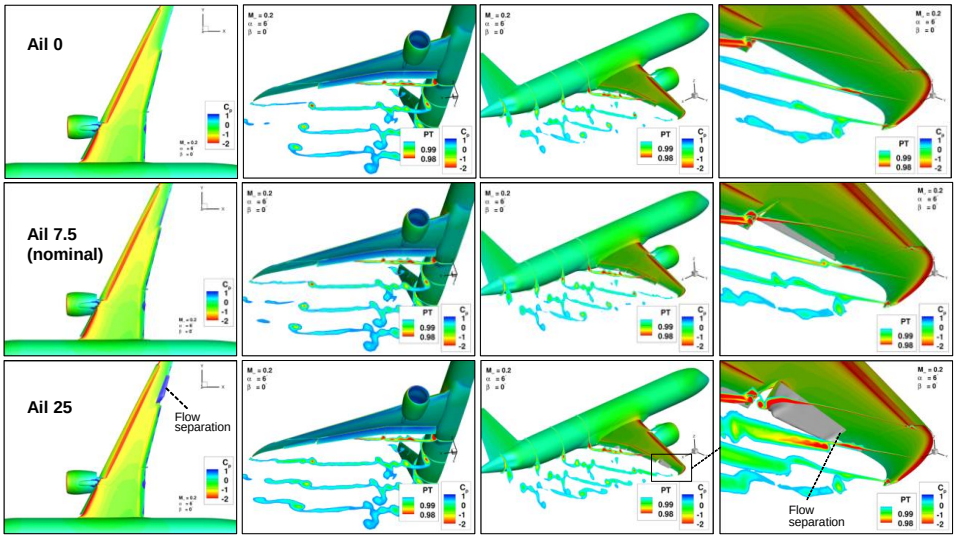

Fig. 4 Baseline flows fields for the different aileron deflections at the nominal takeoff condition (α=6°).

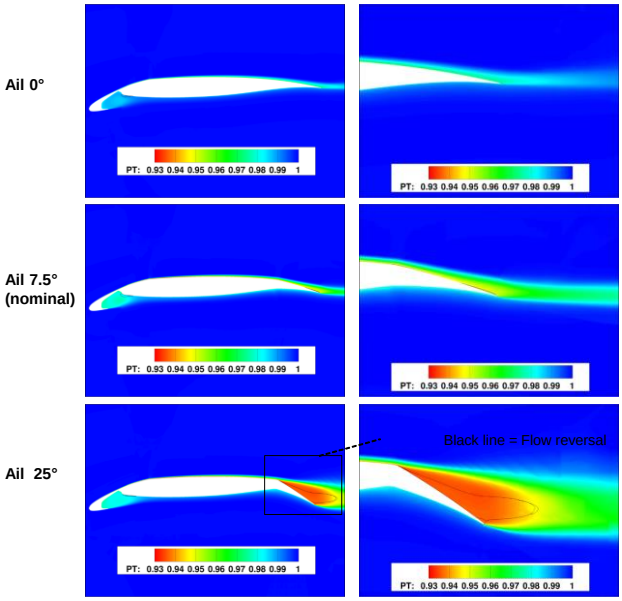

Fig. 5 Baseline flow: total pressure contours at the midaileron cross-sections.

Figure 6 presents the spanload and the pressure distributions at the midaileron sections. The higher aileron deflections help increase the wing loading in the aileron span segment. This loading augmentation extends toward the tip due to the wing sweep. The sectional pressure distributions indicate that as the aileron is deflected the increased wing camber results in increased global circulation affecting the entire wing section, and hence higher sectional lift. As the aileron is deflected to higher angles, the flow starts to separate and drag becomes significant. This is clearly shown in the aerodynamic performance in Fig. 7, where the drag increment at large deflections is such that L/D drops at around 10°. Here the dashed lines denote the nominal aileron deflection of 7.5°. The goal is to augment L/D beyond the level achieved with the nominal aileron deflection by using larger aileron deflections in conjunction with flow control. Specifically, AFC will be used to lower the pressure drag by reducing flow separation, and the induced drag through spanload redistribution.

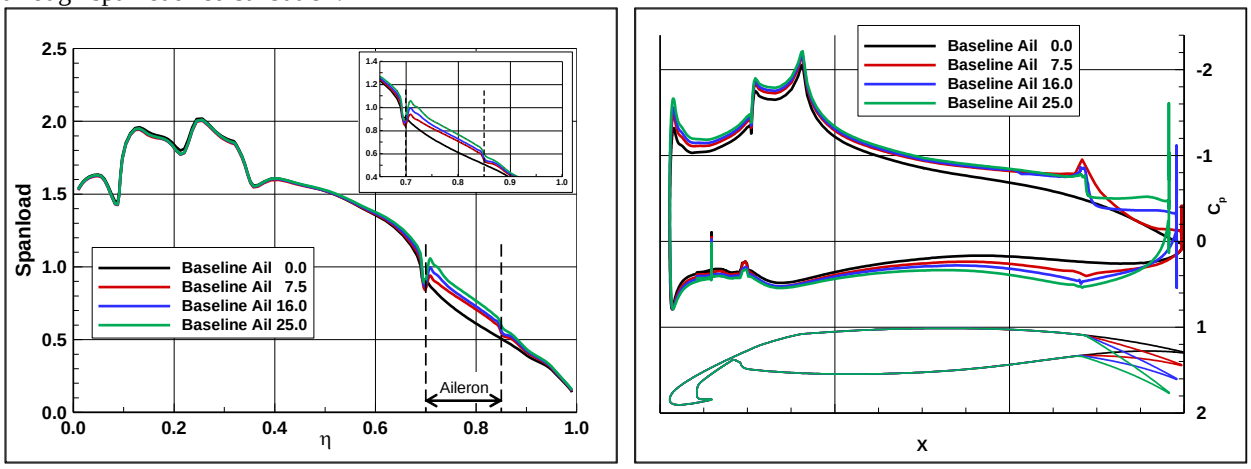

Fig. 6 Baseline flow: spanload and pressure distributions at the midaileron sections.

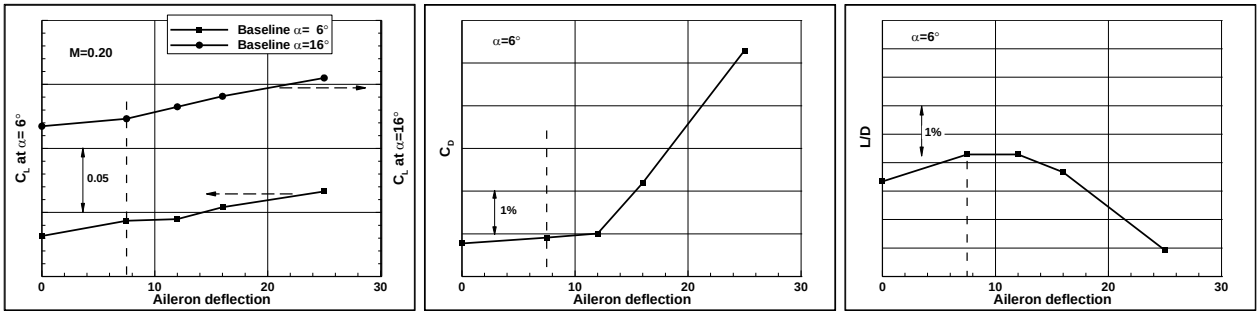

Fig. 7 Baseline flow: aerodynamic performance as function of aileron deflection.

B. Surface Blowing

Since AFC analyses place considerable demands on computational resources, it is necessary to adopt a systematic approach that is practical, with the goal of quickly identifying the most effective AFC implementations. The analysis process evolved through a sequence of progressively complex flow control representations, starting off with surface boundary conditions, up to systems that include dozens of discrete nozzles. Selected results illustrating the design process are discussed hereafter.

A set of flow control cases utilizing constant surface blowing is first considered. This is a quick step that helps guide port placement and orientation of the blowing jets. Surface boundary conditions are applied on the outer mold line of the wing, where the blowing velocity is defined by the mass flow rate and the stagnation pressure and temperature. The actuation is applied just downstream of the aileron hinge line. The blowing jets are perpendicular to the respective hinge lines (when viewed from the top) and they create an angle of 25° relative to the local surface tangent. A very fine grid block is placed in that region for the application of the blowing jet and for capturing the interaction between the jet and the surrounding flow. This block extends from around the midchord station on the wing upstream of the aileron and extends beyond the aileron trailing edge. The boundary condition is applied on a narrow strip of constant width of 0.22% of wing chord length at the midaileron station. The strip contains 16x170 cells in the streamwise and spanwise directions, respectively. The grid consists of 76 million points and 211 subgrids. This

modeling approach is illustrated in Fig. 8 for an aileron deflection of 25°. All solutions using the surface blowing are obtained for the 25° deflection.

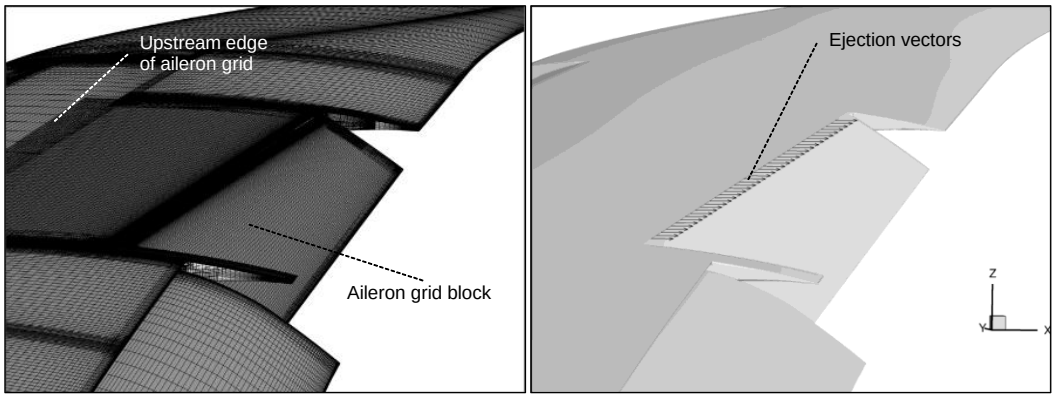

Fig. 8 Approach for the modeling of surface blowing jets.

Figures 9 through 11 present the results of a jet that spans the entire aileron, pointing in the x-direction with a pressure ratio PR=2 and temperature ratio TR=1. TR=1 will be used in all actuation patterns throughout this report, unless otherwise noted. The flow field in Fig. 9 was obtained at α=6° and it is compared to the baseline cases for the aileron at 7.5° and 25° from Fig. 4. This particular jet is very effective in eliminating the flow separation. The intensity of the aileron vortex sheet is considerably reduced. The two distinct tip vortices are the results of the increased loading on the aileron. The total pressure contours at the midaileron section in Fig. 10 show that the circulation produced by the streamlining effect at the aileron affects the entire flow field, including the slat cove. The blowing jet affects the flow upstream of the hinge line, where the thickness of the viscous layer is noticeably reduced. The impact of AFC on the aerodynamic performance is shown in Fig. 11. Flow control results in increased lift over the entire range of incidences, including C_{Lmax}. The spanload obtained with flow control, which is closer to an elliptical distribution, and the reduced separation result in lower drag. This results in significantly higher L/D. The increased loading at the aileron results in a nose-down pitching moment, resulting in a potential trim drag penalty that needs to be accounted for. It is noted that the drag levels throughout this CFD report are untrimmed. Trim drag effects are addressed in the integration study of the companion paper [7].

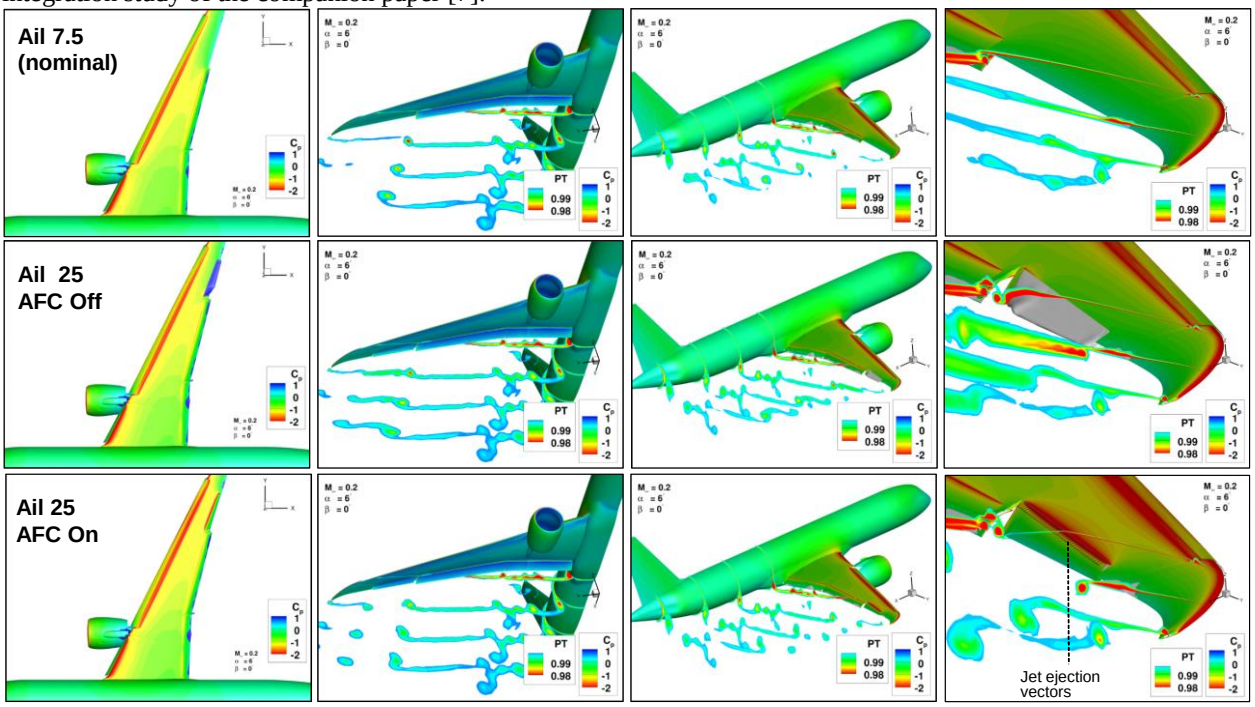

Fig. 9 Flow fields for the nominal 7.5° aileron deflection, and the baseline and AFC actuation for the 25° aileron deflection (α=6°).

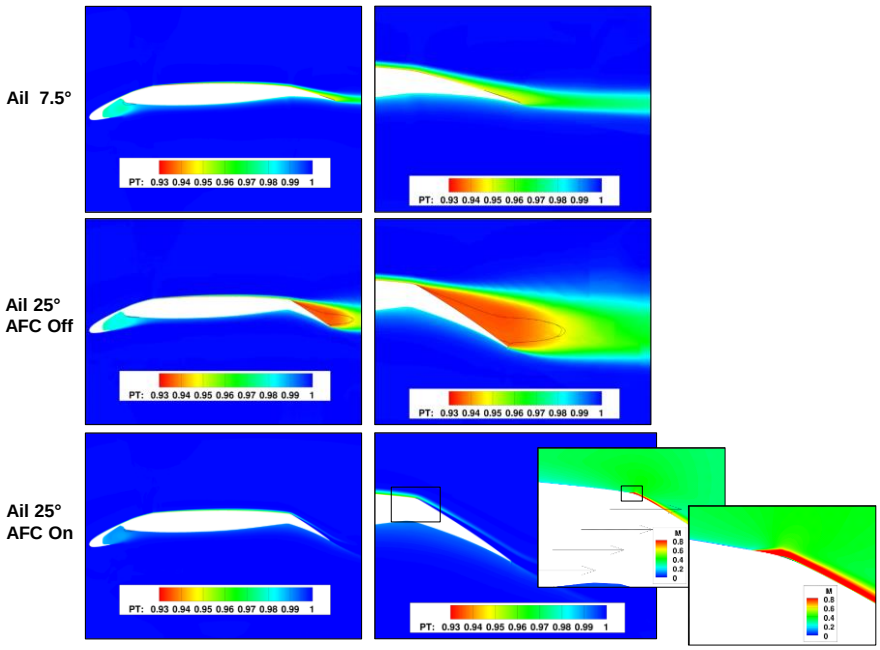

Fig. 10 Flow fields at the midaileron section for the cases in Fig. 9.

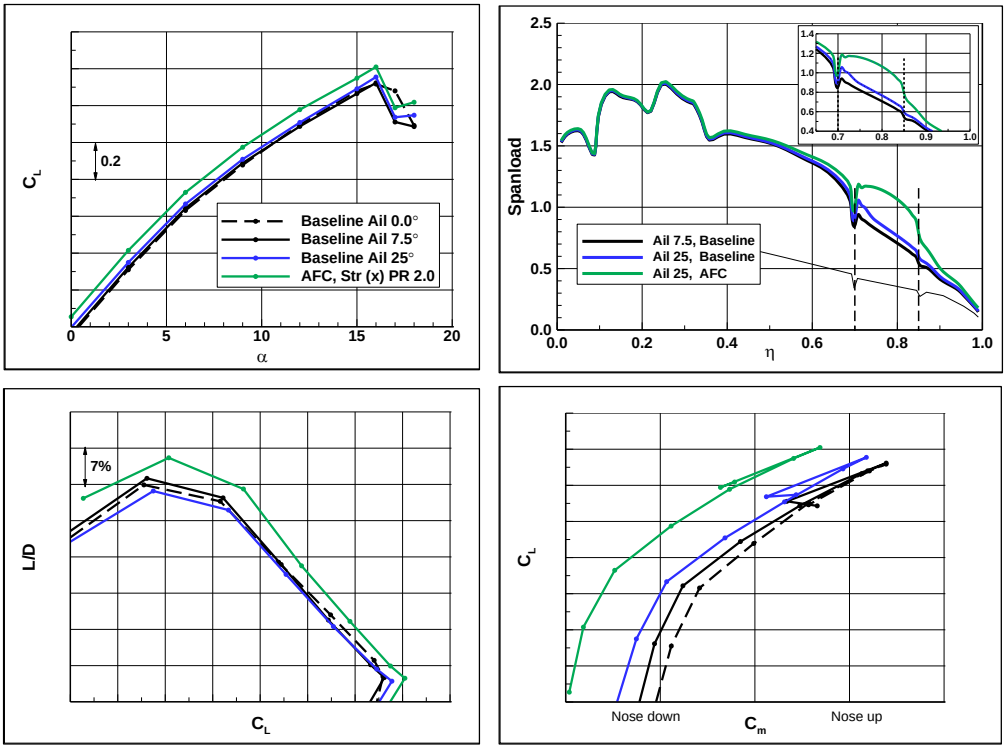

Fig. 11 Aerodynamic performance due to jet with PR=2.

The sensitivity to jet intensity is analyzed in Figs. 12 and 13 at α=6°. Here the PR varies from 1.05 to 2. Relative to the baseline case, the addition of momentum with increased actuation intensity helps to gradually attach the flow. The flow is effectively attached at a relatively low PR of 1.2. The increased camber effect results in added lift in the outboard wing segment. Combined with the reduction in drag, flow control results in improved L/D over the input pressure range. As the pressure ratio increases, the forces and moments increase as depicted in Fig. 13. Choosing the best actuation parameters for an efficient and practical flow control system is a critical design criterion and it will be the central theme throughout the remainder of this paper.

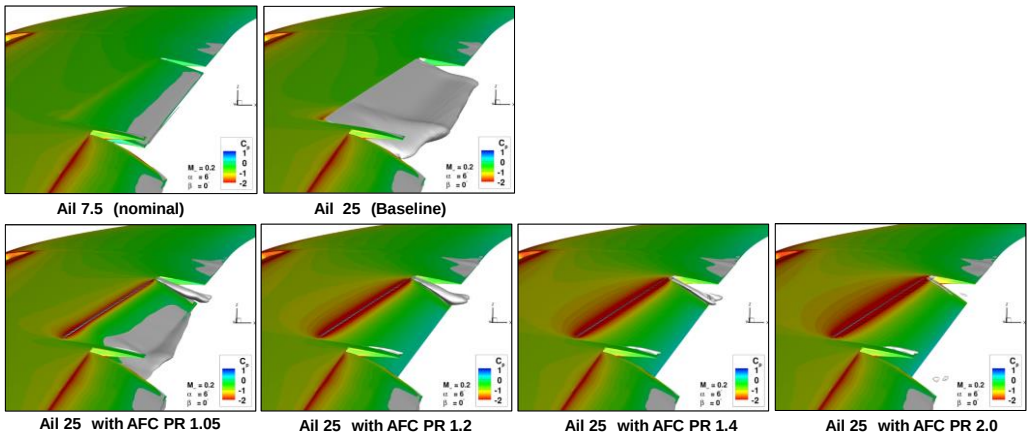

Fig. 12 Sensitivity to actuation level.

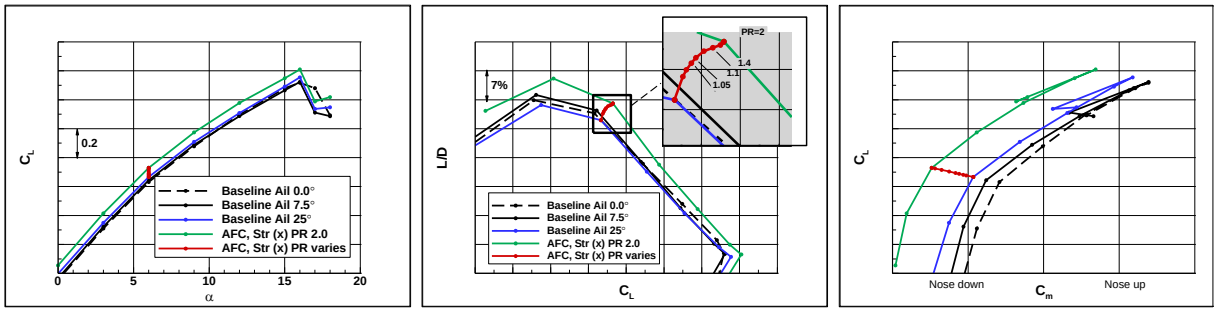

Fig. 13 Effect of actuation intensity on aerodynamic performance.

In the analysis of AFC systems, it is instructive to refer to the corresponding inviscid flow. The inviscid lift determines the theoretical upper limit of an airfoil to produce lift in the absence of viscous effects. Consequently, the inviscid lift level can be used as a yardstick for AFC efficiency. Throughout the following analysis, the inviscid lift is used to gauge the performance of the various actuation patterns.

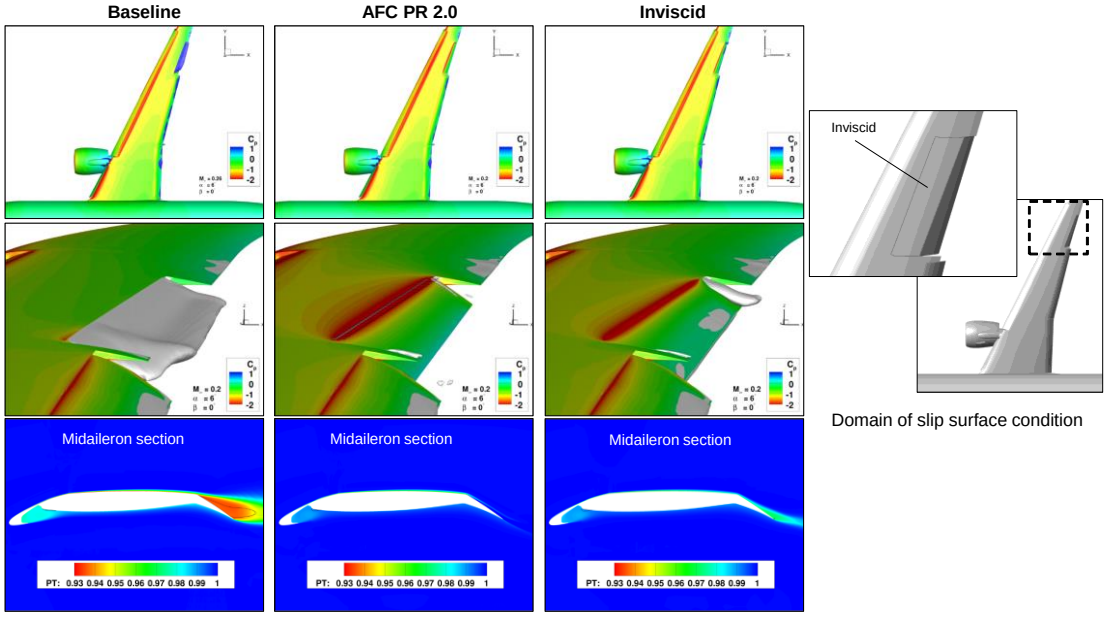

Fig. 14 Pseudo-inviscid flow is used to gauge the efficiency of flow control.

Since the flow control is applied locally, a special modeling procedure has to be devised to establish a comparable inviscid limit. This pseudo-inviscid model uses a slip surface condition on the upper surface of the aileron and on

portion of the wing ahead of the hinge line. This strategy is illustrated in Fig. 14, together with the flow fields obtained for the 25° aileron. It is noted that the inviscid solution results in a very small separation pocket, likely due to the numerical dissipation. Based on these solutions, the actuated flow with PR=2 produces a flow that is more effective than the inviscid case. The jet is strong enough to suppress separation and provide added circulation beyond the inviscid level. This is also evident from the wing load distributions and the sectional pressure plots in Fig. 15.

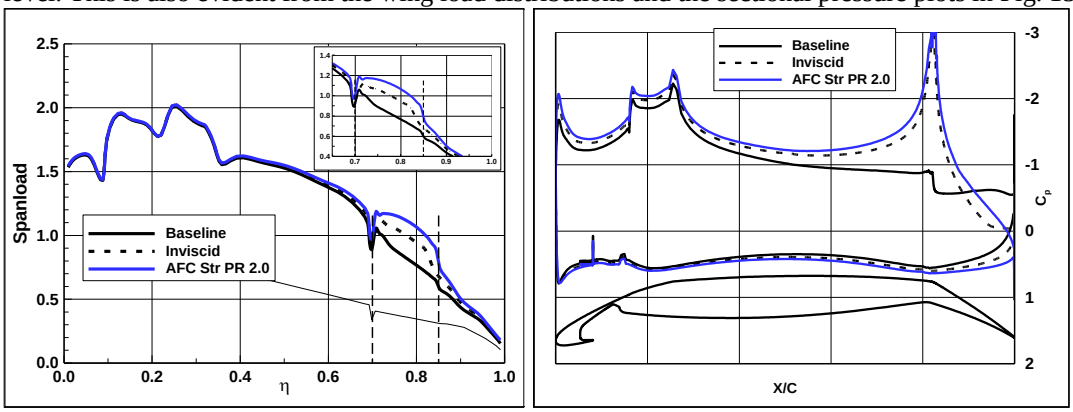

Fig. 15 Aerodynamic characteristics of the wing for the pseudo-inviscid and the actuated PR=2 case.

The aerodynamic performance as function of actuation mass flow coefficient C_q is shown in Fig. 16. The lift is obtained at α=6° and the percentage increment in L/D due to AFC is taken relative to the corresponding baseline C_L. The baseline (unactuated) aileron 25° results in higher lift relative to the nominal aileron, but it comes with higher drag, as indicated by the drop of about 1% in L/D. However, flow control makes up for this shortfall with a very small pressure ratio. As input pressure becomes larger, the incremental lift and L/D become substantial. Using the inviscid level as a measure of efficiency, it becomes apparent that PR can be dialed down for more efficient actuation. Flow control is very effective in reducing viscous effects and suppressing separation up to a PR of about 1.2, and it becomes less efficient at higher pressure where actuation becomes a mechanism of circulation control beyond the inviscid limit. It is pointed out that the C_q is small since it is being referenced to the wing area and it represents actuation input for both ailerons. Also, C_q of 0.00018 corresponds to the mass flow that could potentially be supplied by an APU (marked by the vertical dash line).

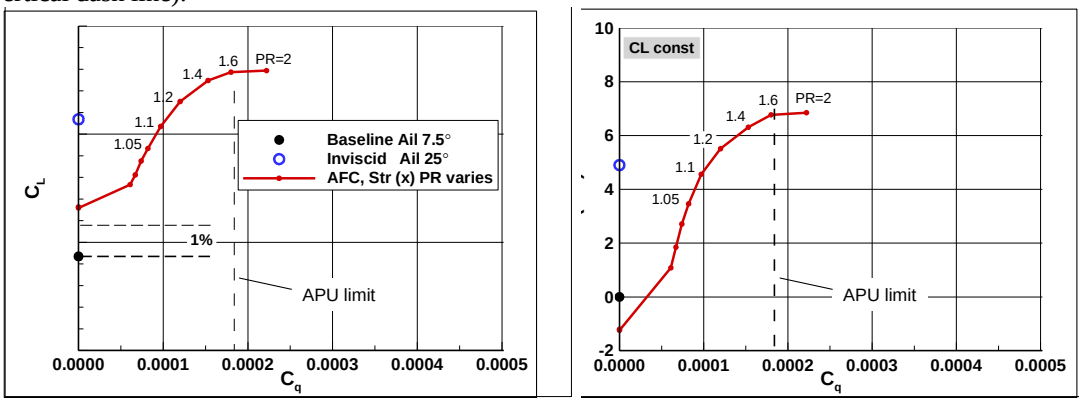

Fig. 16 Aerodynamic performance as function of actuation input, aileron 25°.

Several actuation patterns are considered next. The first is spanwise actuation because it relates to an important integration aspect. The space available for installing the AFC system close to the aileron and the neighboring area is limited. It is therefore instructive to evaluate the effect of AFC relative to span placement. Figures 17 and 18 show the effect of actuation of PR=2 on the inboard (IB) half span vs the outboard (OB) half span segments of the aileron. Results indicate that the actuation has a local effect on the separation pattern and the aerodynamic gains in terms of L/D are quite similar, with a slight advantage to the inboard actuation. This is likely due to the spanwise effect on swept wings where perturbations propagate outboard toward the wingtip as can be inferred from the spanload distributions. Both of these actuation patterns are less efficient than the entire span actuation (Fig. 18). It is noted that there are implications to structural integrity of the aileron and its mechanical actuators particularly under the added load from different actuation patterns.

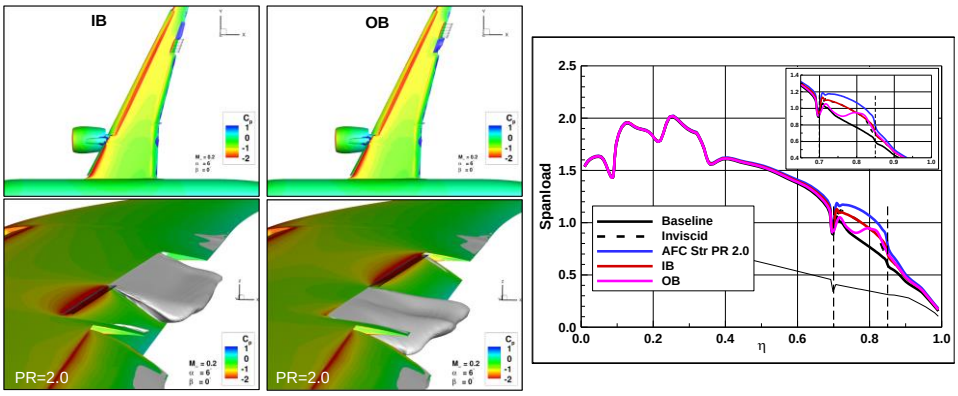

Fig. 17 Inboard versus outboard aileron actuation, aileron 25°: surface flow characteristics and separation patterns.

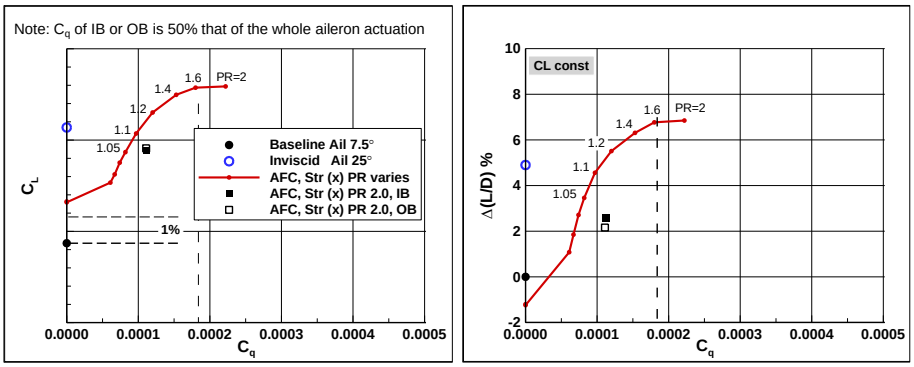

Fig. 18 Inboard versus outboard aileron actuation, aileron 25°: aerodynamic performance.

Jet angle to local surface is investigated next in Figs. 19 and 20. The jet angle is measured relative to the x-coordinate, so in the previous actuation modes the angle is 0°. Jet angles of +10° and -10° were analyzed, which correspond to 22° and 2° off the local surface tangent, respectively. In this analysis using a surface boundary condition that is applied on a constant strip width, when the jet angle varies, the mass flow changes according to $\dot{m} = \rho \mathbf{U} \cdot \mathbf{A}$, where **U** and **A** are the velocity and area vectors, respectively. For example, when the jet is perpendicular to the strip, $\dot{m}$ is maximum. As the jet becomes tangent to the surface, $\dot{m}$ becomes very small. This is illustrated in Fig. 19, which shows the flow fields in the midaileron section in terms of total pressure and Mach number. Figure 20 reveals that the jet effectiveness increases with smaller jet-to-surface angles. When the jet angle is large, low velocity jets are ineffective, whereas low angle jets affect the flow even at very low pressure ratios.

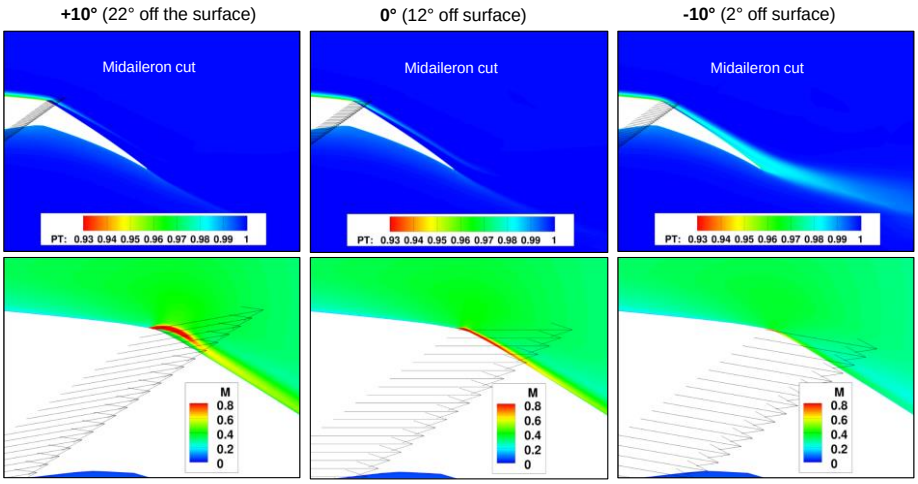

Fig. 19 Effect of jet ejection angle, aileron 25°: flow field.

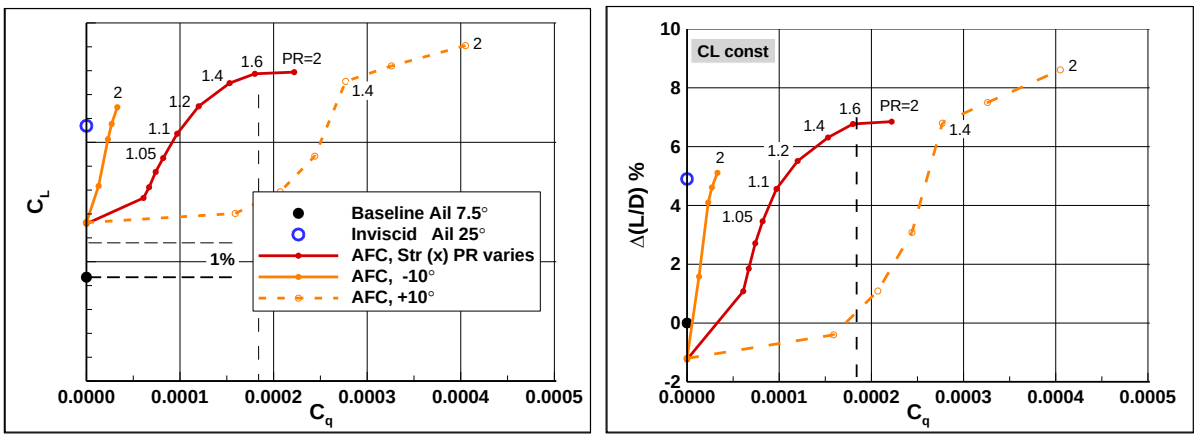

Fig. 20 Effect of jet ejection angle, aileron 25°: aerodynamic performance.

A segmented AFC application is analyzed in Fig. 21 for PR=2 and -10° exit angle, based on the aforementioned convention. There are 11 discrete jets of the same width, spread at equal distances across the aileron span. This actuation exhibits an alternating pattern of separated and attached regions which are coincident with the unactuated and actuated span segments, respectively. The discrete jets result in a wavy wing load distribution. The segmented AFC pattern in not as efficient as the full span actuation.

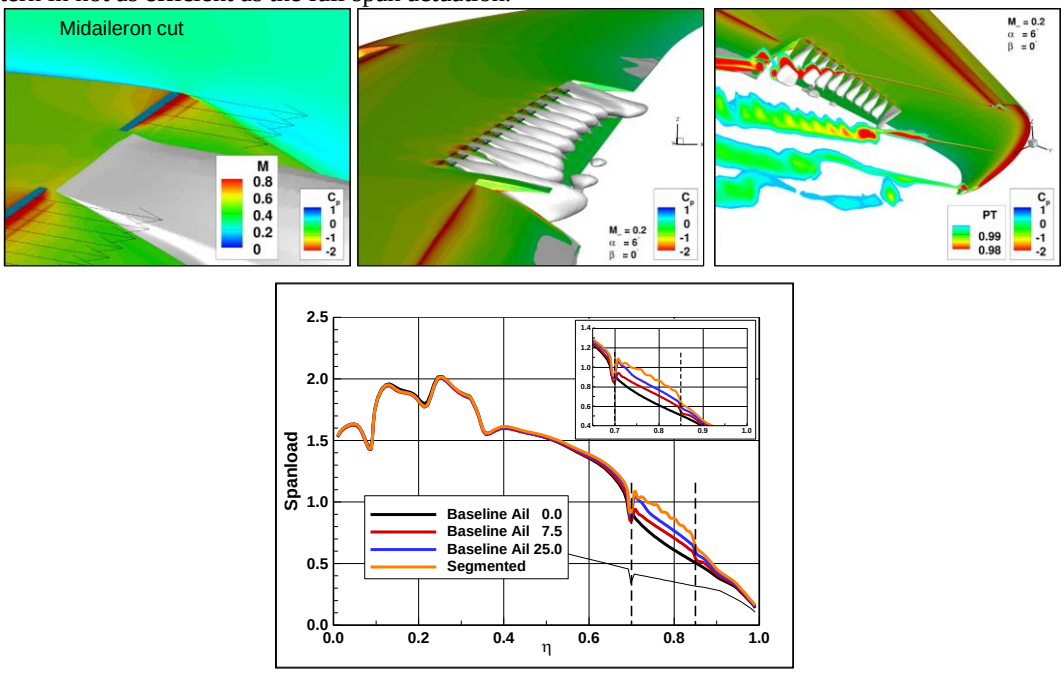

Fig. 21 Segmented AFC application, aileron 25°, PR=2, jet angle -10°.

C. Blowing Nozzle

After getting insight into the effects of actuation parameters and placement using the simplified modeling approach in the previous section, a more realistic implementation of flow control is now considered. It consists of a continuous nozzle that runs the full span of the aileron. The long nozzle system is described in the inset in Fig. 22. It consists of a two-dimensional convergent-divergent (CD) section in the vertical plane (xz) whose exit section forms a long slot along the aileron. The throat to inlet area ratio, A_{th}/A_{in} is 0.4. The inlet consists of a constant area duct, which is connected to a convergent duct section. The diffuser is long enough to ensure that its half angle is smaller than 15° to prevent the flow from separating. The nozzle cross-section is identical along the span. The grid system consists of 85 million points. The solution for PR=2 is also shown in Fig. 22. At this pressure ratio, the CD nozzle becomes choked. The flow accelerates in the diffuser and the jet is ejected at supersonic velocity over the aileron. At this condition, the blanket of high speed flow helps energize the viscous layer and prevents flow separation over the entire aileron.

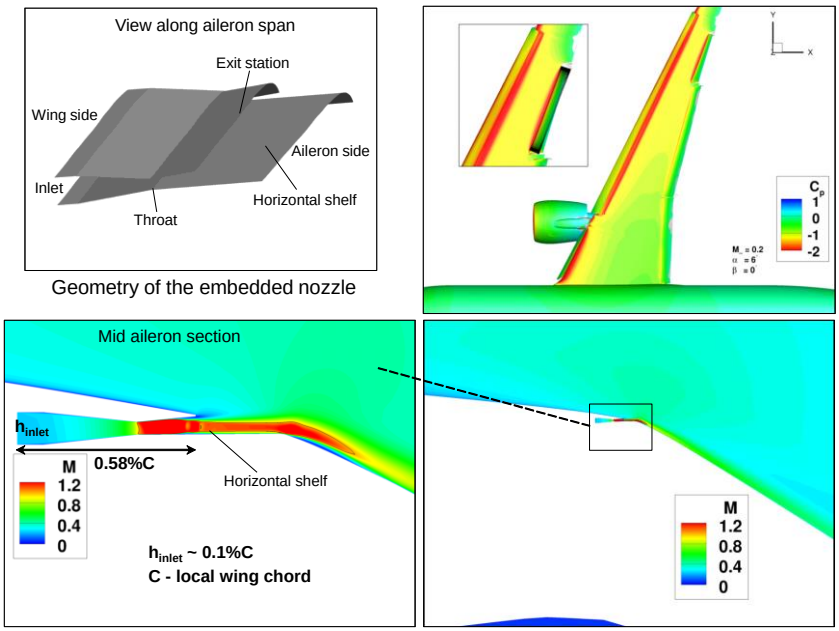

Fig. 22 Blowing convergent-divergent nozzle, aileron 25°, PR=2.

It is interesting to see the differences in the results obtained with the surface blowing and the CD nozzle. The cross-sectional Mach number contours indicate that at some distance from the outer mold lines the flow fields look very similar for both pressure ratios. The more realistic representation of the jet with the CD nozzle shows a higher efficiency in terms of L/D across the pressure range. Figures 23 and 24 show the effect of input pressure ratio. Here the black lines denote sonic conditions. As PR increases, the nozzle becomes choked and supersonic velocity is attained in the diffuser and beyond. The jet expands as it reaches the aileron surface and accelerates as it emerges over the upper surface of the aileron.

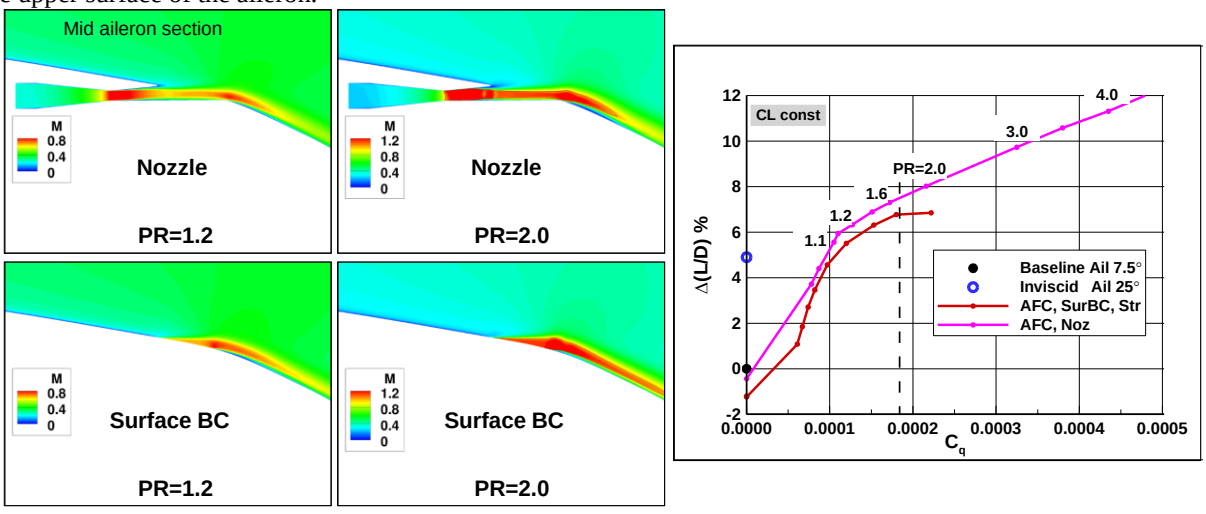

Fig. 23 Solution comparison between the surface boundary condition and the blowing nozzle, aileron 25°.

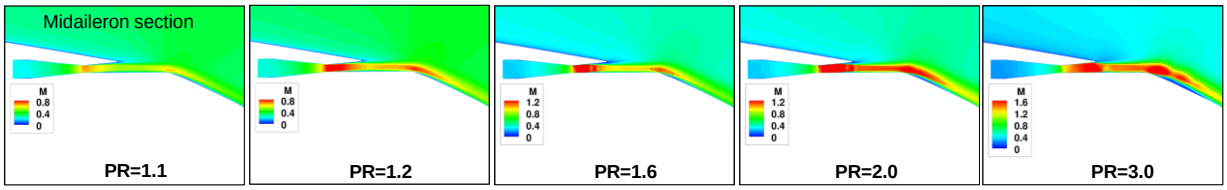

Fig. 24 Effect of pressure ratio of the blowing nozzle, aileron 25°.

Driven by integration issues such as space availability and breach of the wing and aileron outer mold line (OML), an assessment of nozzle size was conducted. The size of the original nozzle was reduced by a factor of two, to produce two sequentially smaller nozzles having identical area ratios. Denoting the original nozzle as nozzle 100%, the smaller nozzles are dubbed nozzle 50% and nozzle 25%. Nozzle layouts and sample solutions obtained for PR=2 are presented in Fig. 25. The nozzles span the entire aileron and their exit station is at the same streamwise location. All three nozzles are effective in reducing flow separation. The flow fields within the nozzle are very similar since the nozzle area ratio is the same. Figure 26 shows the relative efficiency of the different sized nozzles. Although the smaller nozzles are more efficient, they require higher PR. Ultimately the AFC integration and the available air sources (PR, $\dot{m}$) will drive the selection of the nozzle size.

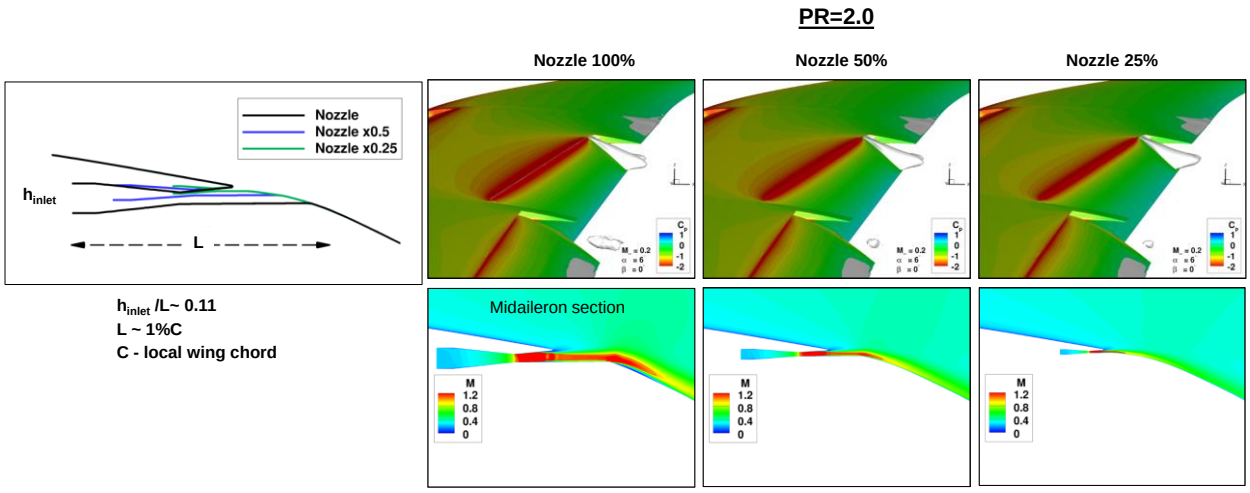

Fig. 25 Effect of nozzle size on flow field, aileron 25°, PR=2.

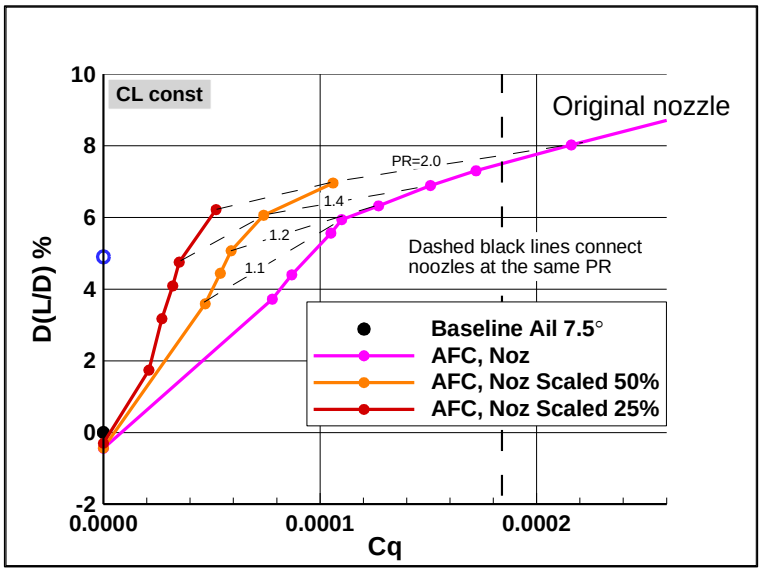

Fig. 26 Effect of nozzle size on aerodynamic performance, aileron 25°, PR=2.

D. Discrete Blowing Nozzle

Systems of discrete actuators were also considered for the aileron application. An array of actuators in the form of CD nozzles, where the sectional geometry is defined in the horizontal plane xz, is used here. The geometry of the actuators is identical and of the same size, with throat to inlet area ratio of 0.4, identical to that of the blowing nozzle. The nozzles are spaced at equal distances along the aileron at the same location as the blowing nozzle. The centerlines of the nozzles are perpendicular to the hinge line. Two layouts were considered for the computational assessment of the discrete nozzles. One consists of 78 nozzles with an aspect ratio of 2 at the throat section of each nozzle, where the shorter dimension is vertical. The other set uses an array of 63 nozzles with aspect ratio of 3. The two layouts are

denoted AR2 and AR3. The throat area A_{th} of each nozzle is the same in both layouts. Therefore, the ratio of total throat area between AR2 and AR3 is 1.24. These arrangements are described in Fig. 27, where the blowing nozzle 100% from the previous section is included for reference. Note that the exit stations of the nozzles lie on a backward facing step. The step size is identical but nozzle height is different. Each of the grid systems of these configurations consists of about 86 million points.

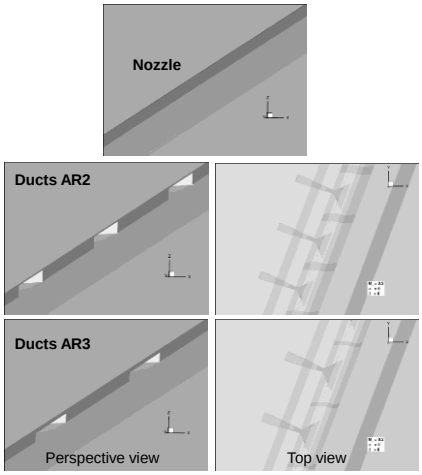

AR (at throat)	# nozzles per aileron	A_{th} per nozzle	A_{th} total
2	78	A_{th}	$78 \cdot A_{th}$
3	63	A_{th}	$63 \cdot A_{th}$

Fig. 27 Layouts of the discrete nozzle.

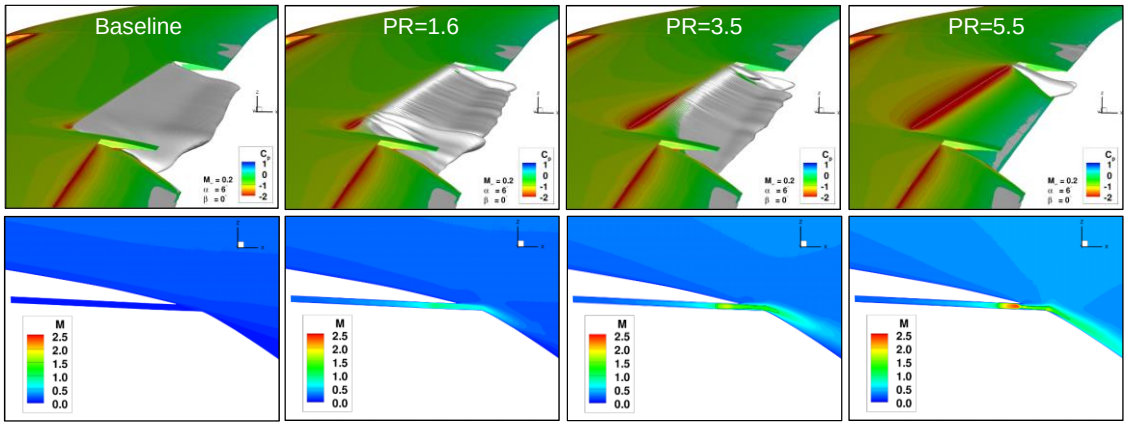

Fig. 28 Flow fields of the discrete nozzles AR2, aileron 25°.

Figure 28 shows the flow fields obtained for the AR2 layout at different input pressure. Cross-sectional cuts through one of the actuators are also included. As PR increases, the actuators become choked and the supersonic jets start affecting the separation bubble. The AR2 pattern is very efficient, but because the total throat area is very small, it requires high PR. Even at the highest PR of 5.5, a sliver of separated flow still exists at the trailing edge of the aileron. Performance comparison of AR2 and AR3 and the blowing nozzle is presented in Fig. 29. Both actuation layouts are effective, but from the separation patterns in the PR=5.5 cases, it appears that AR2 has an advantage, likely due to its larger area. The aerodynamic performance of the family of blowing nozzles and the discrete nozzles are summarized in Fig. 30 as functions of C_q and the momentum coefficient, C_μ (integrated at the throat section). Interestingly, the various curves are fairly clustered in the C_μ plot, reinforcing the notion that the momentum coefficient is the relevant AFC parameter for the kind of flows considered here. Clearly both nozzle families are potential candidates of actuators as they require mass flows well within the capability of an APU or another equivalent source for producing meaningful L/D gains. Irrespective of the type of nozzles, better mass flow efficiency is achieved with smaller area actuators, but they require higher PR. These types of trades are a central element in the design of a practical AFC system. Figure 31 summarizes the major trade factors for the type of nozzle candidates used in this

study. Aspects of system integration that considered actuator sizing, the pairing up with potential sources, as well as other factors, are addressed in the companion paper [7].

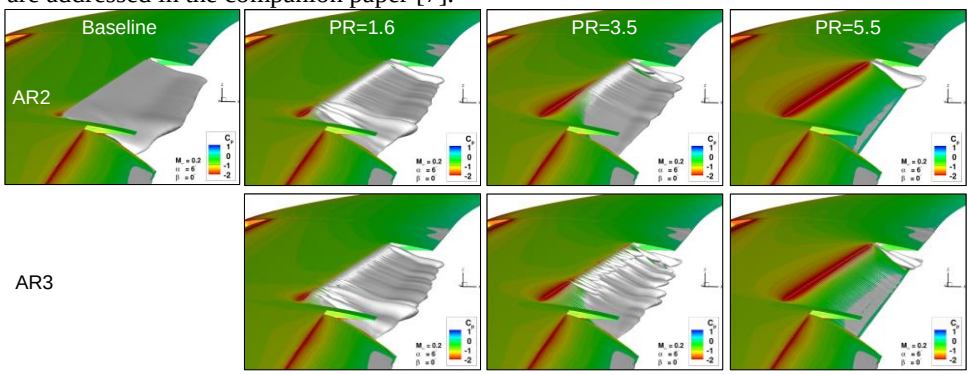

Fig. 29 Flow fields for the discrete nozzle layouts, aileron 25°.

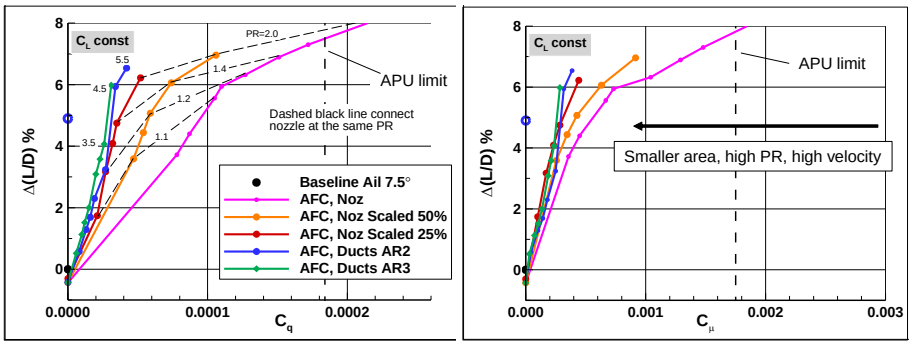

Fig. 30 Aerodynamic performance of the blowing nozzles and the discrete nozzles, aileron 25°.

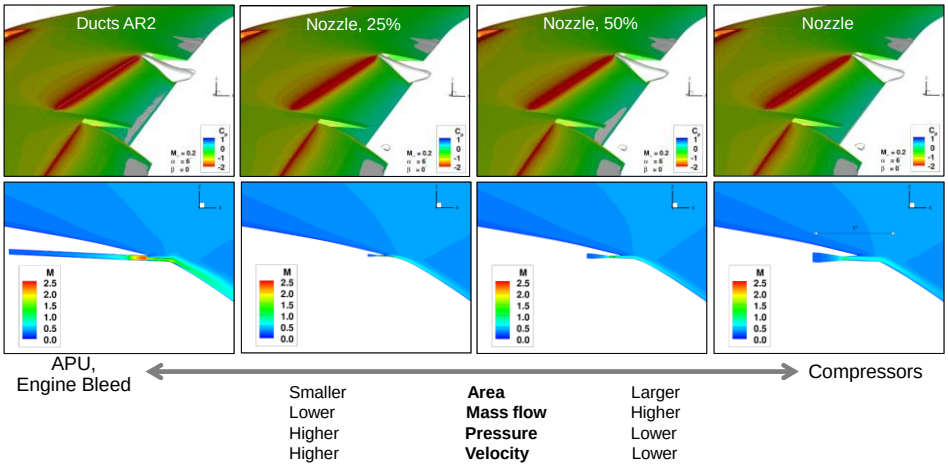

Fig. 31 Trade factors that will impact the practical design of AFC.

The manner in which integration factors and power sources might determine the type of actuation is illustrated in Fig. 32. It presents the results of some of the nozzles discussed earlier in terms of the gain in L/D and C_q required for actuation as functions of PR. For example, if the design target is an increase of 6% in L/D, two optional layouts might be considered. One scenario denoted 'A' might employ a system of discrete nozzles AR2 with a high PR source of 4.5, which requires limited mass flow. The option marked 'B' uses the blowing nozzle 50% with PR=1.4. Scenario 'C' represents a low-PR, low-C_q system with 1.3 and 0.00003, respectively, which is based on nozzle 25% and attains a 4% improvement in L/D. Finally, it is pointed out that although all these scenarios are within the limits of an APU in terms of mass flow, the maximum pressure available at the inlet of the actuators is unknown. That will depend on the distance from the source to the actuators, the plumbing system and other factors. These considerations will be discussed by Vijgen et al. [7]

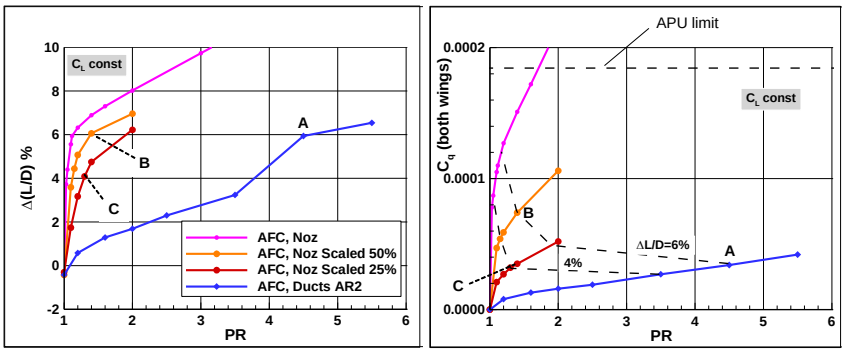

Fig. 32 Trade factors for the various nozzles configurations.

E. Actuator Efficiency

It is instructive to compare the efficiency of the actuators with respect to their internal flow. Gas dynamics (GD) for the one-dimensional (1D) inviscid flow in nozzles having comparable area ratios is used to gauge effectiveness for a set of blowing nozzles considered in previous sections. This will provide the flow properties of the comparable ideal flow with no losses. Figure 33 shows the actuation coefficients as a function of PR and the dash curves are the GD counterparts. Generally, all nozzles exhibit good quality flow for all nozzle shapes, especially at PRs higher than about 1.5. The difference between the theoretical and the computed flows are due to viscous losses and deviations from the 1D flow. The differences in efficiency of the nozzles are presented in Fig. 34, using the ratios of the computed to the ideal GD values of the actuation parameters C_q and C_μ. This efficiency measure is plotted against the total area of the throat sections for each of the nozzle layouts. The computed trends indicate that the smaller the actuators, the bigger losses are. A plausible reason is that in small actuators the viscous boundary layers occupy a bigger fraction of the cross-sectional area.

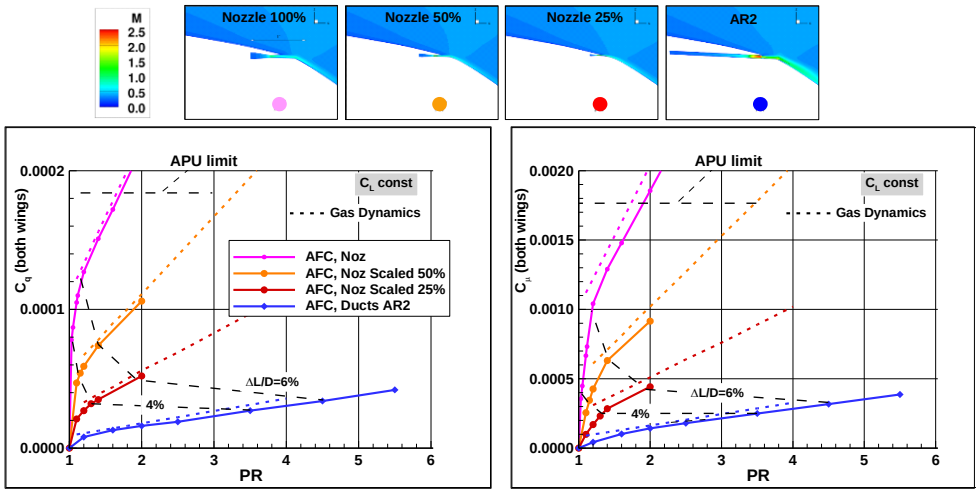

Fig. 33 Actuators efficiency for a set of blowing nozzles.

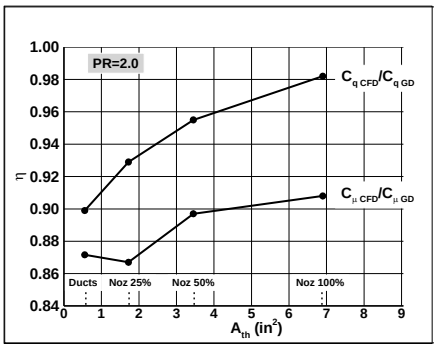

Fig. 34 Actuators efficiency for a set of blowing nozzles.

F. Aileron Deflections

The AFC simulations presented in the previous sections were performed for an aileron deflection of 25°. At this point, more practical aileron deflections will be considered as lower deflections are more consistent with the designs of current airplanes. Smaller deflections will result in lower loads, and hence more acceptable hinge moments for the aileron mechanical actuators to handle. Moreover, this may lead to reduced wing twist and bending moments, as well as lower trim drag.

For ease of integration, the analysis is performed for the medium size nozzle of 50%, the cross-section of which is shown in Fig. 35 for the ailerons 16° and 25°. To the extent possible, the analyses use similar grids for the different aileron deflections in order to ensure minimal differences in discretization errors. The baseline flows for α=6° are shown in Fig. 36. Mild separation forms along the trailing edge of the aileron at 7.5°. Flow separation develops over the entire aileron at 16° deflection, with a larger region of flow reversal at 25°. The size of the separation pockets for the set of aileron deflections is also evident from the cross-sectional wake contours of PT. The larger the deflection angle, the thicker and more intense the wake is. The flow fields obtained with actuation of PR=1.4 are illustrated in Figs. 37 and 38 for the progressively higher aileron deflections. The aerodynamic characteristics of the wing for aileron 16° with nozzle 50% at PR=1.4 in Fig. 39 shows the loading in the aileron wing area and outboard, with more elliptic-like load distribution. The L/D improvements from actuation at various PRs in Fig. 40 show that when the aileron is largely separated, the flow control is very effective. The effectiveness drops at the lower deflections, where separation is relatively mild and by and large the AFC benefits are due to circulation control beyond the inviscid limit. All of these results are summarized in Fig. 41.

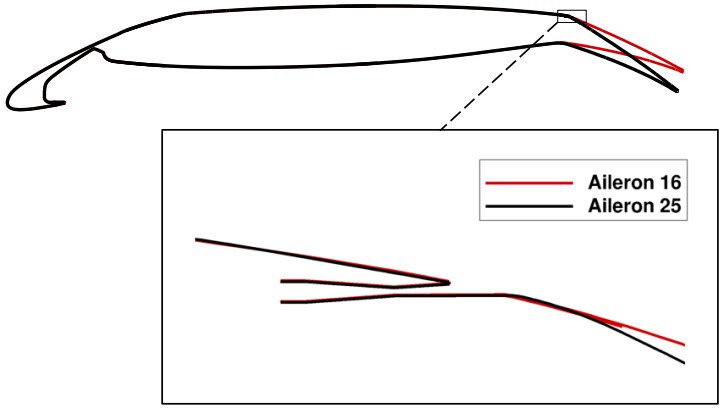

Fig. 35 Nozzle 50% embedded in the aileron 16° and 25°.

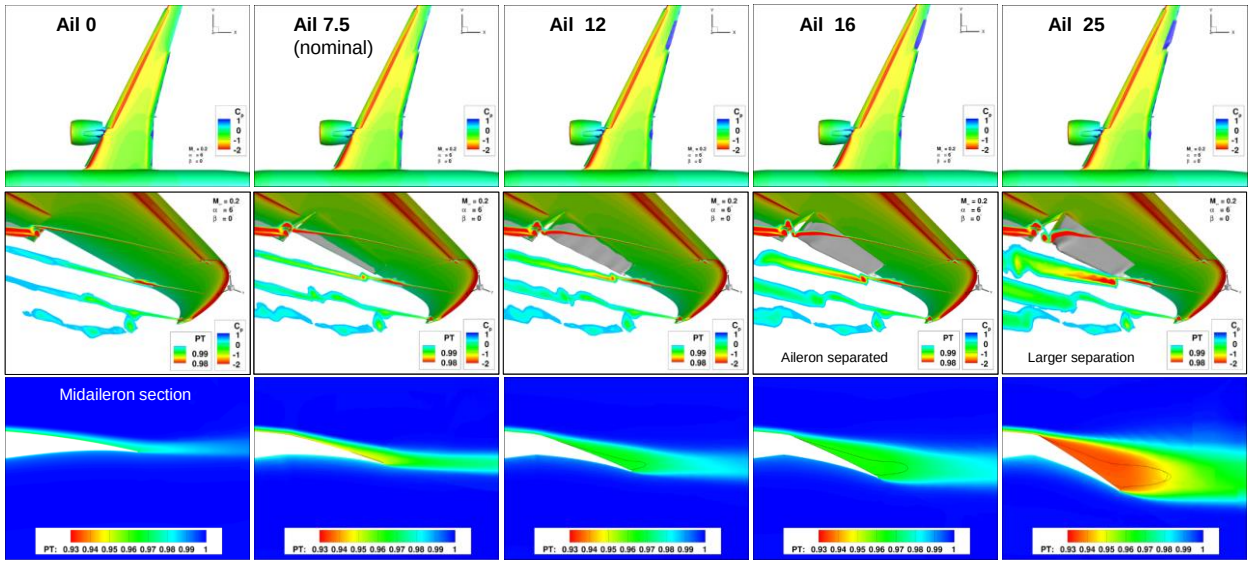

Fig. 36 Baseline flow fields for various aileron deflections, α=6°.

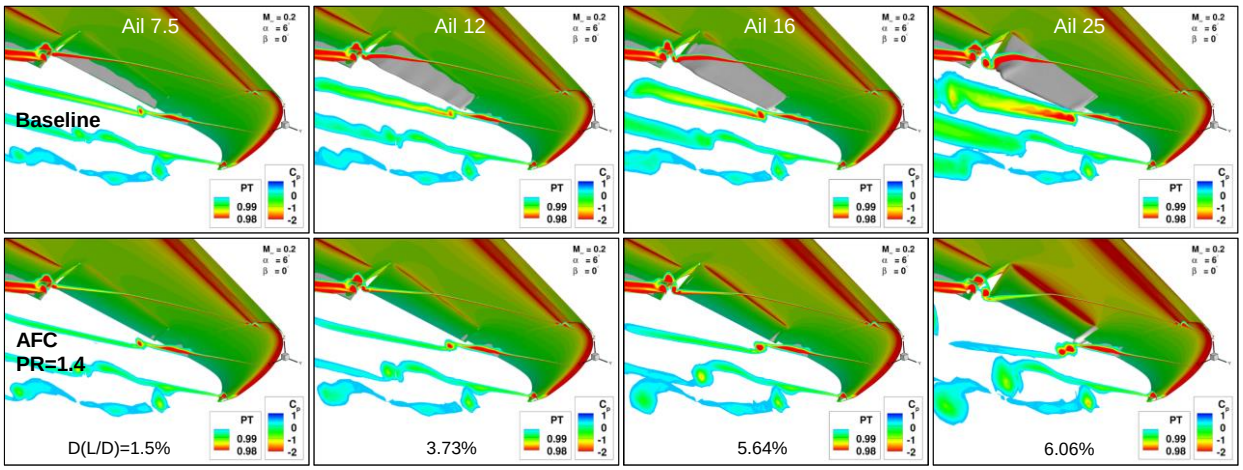

Fig. 37 Flow fields for the baseline and the actuated nozzle 50% at PR=1.4 for various aileron deflections.

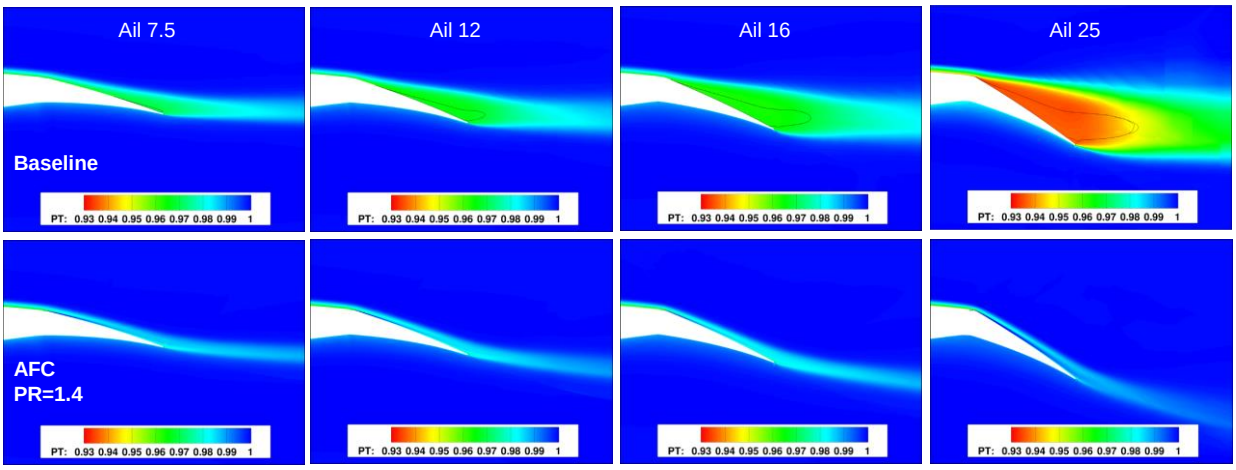

Fig. 38 Flow fields at the midaileron section for the baseline and nozzle 50% actuated at PR=1.4 for various aileron deflections.

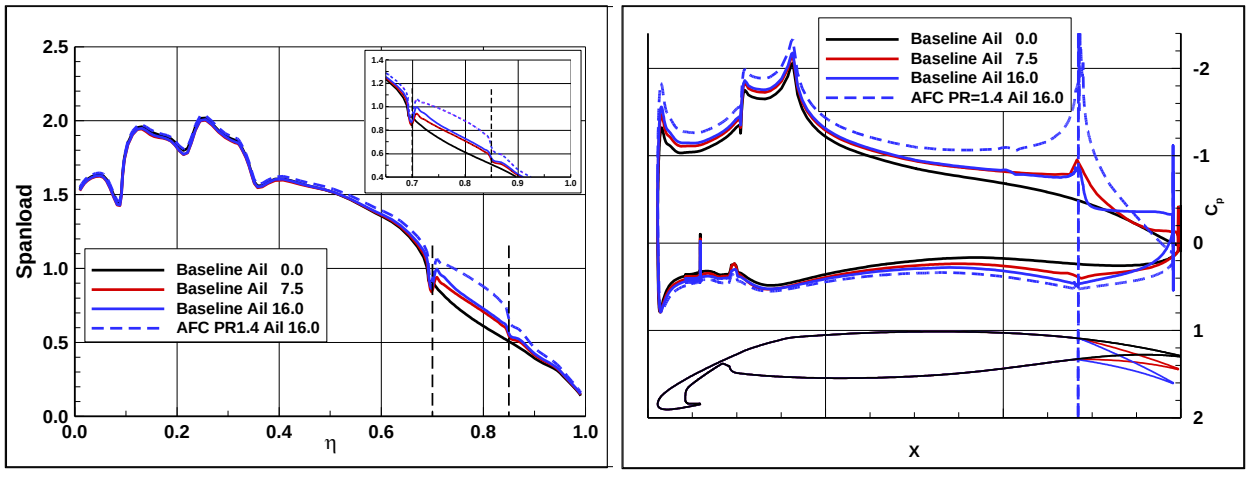

Fig. 39 Aerodynamic characteristics of the baseline for various aileron deflections, and aileron 16° with nozzle 50% at PR=1.4.

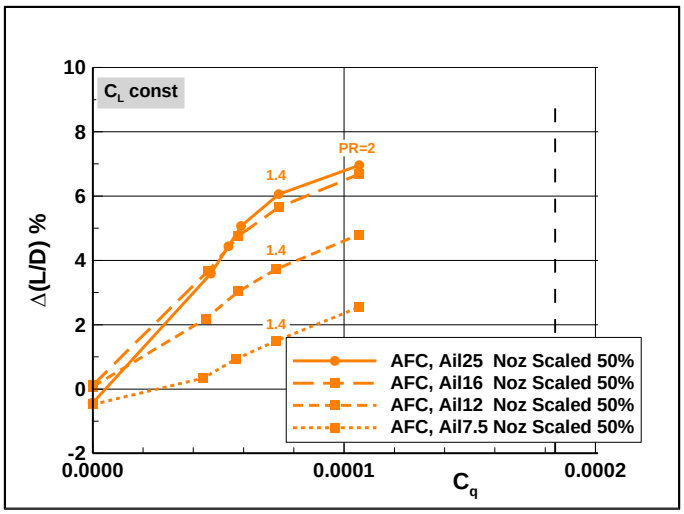

Fig. 40 AFC effectiveness for various aileron deflections.

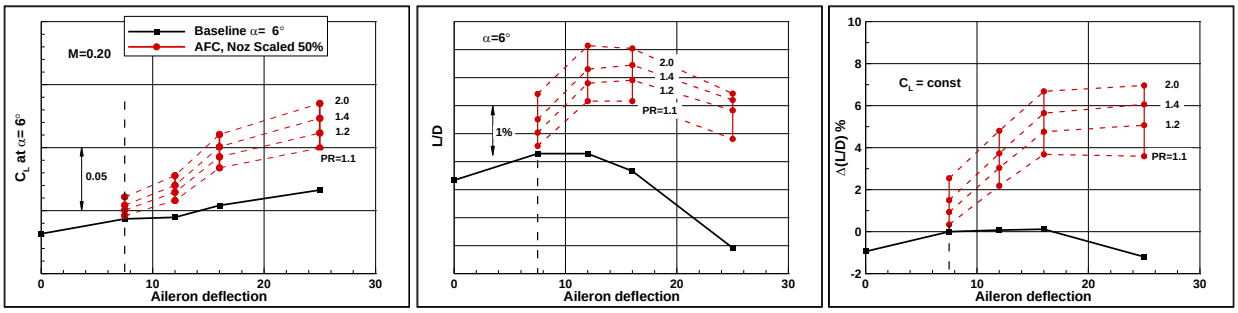

Fig. 41 Aerodynamic performance due to AFC using nozzle 50% as function of aileron deflection, α=6°.

G. Reynolds Number Effects

All the simulations described in the previous sections were obtained for Re=6 million. Results of representative flight conditions for Re=25 million are presented next. Figures 42 and 43 show the Re effects on the performance of the baseline airplane at takeoff for the aileron deflections of 7.5° and 25°. The high Re produces higher lift and lower drag, consistent with the flow fields in the midaileron cuts. The viscous effects are less pronounced at high Re, clearly seen by the thinner boundary layer on the upper wing surface as it passes over the aileron. The effect of Re on AFC is captured in Fig. 44. Commensurate with the smaller viscous effects at high Re, the AFC gains are also slightly smaller across the pressure range. Interestingly, the relative AFC effects depend on PR. Low PR is more effective at high Re because of the thinner boundary layer, as shown in the flow fields in Fig. 45. That is because it takes very little momentum from AFC to affect the flow when the viscous effects are milder. At PR of about 1.2, the situation reverses, whereby larger momentum is more impactful for the low Re case when the viscous effects are greater. Further details on the Reynolds number effects can be found in the complete NASA report [9].

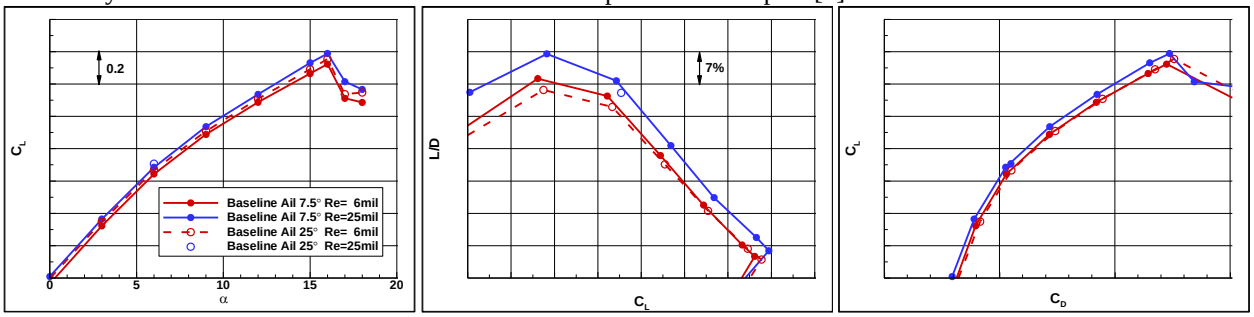

Fig. 42 Reynolds number effects on the performance of the baseline airplane at takeoff for Ail7.5 and Ail25.

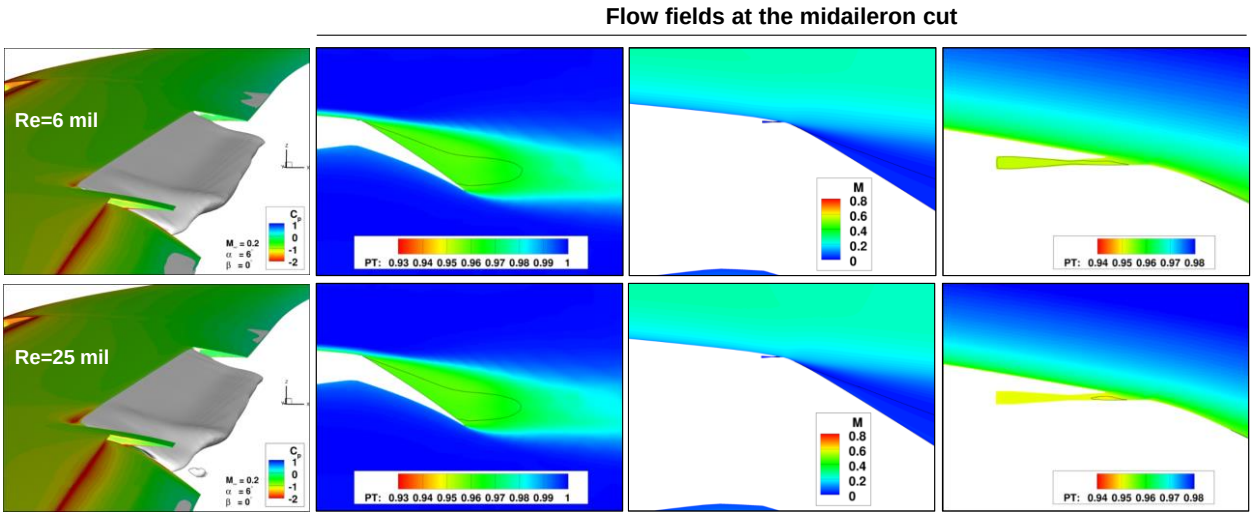

Fig. 43 Reynolds number effects on the flow fields of the baseline airplane at takeoff for Ail25.

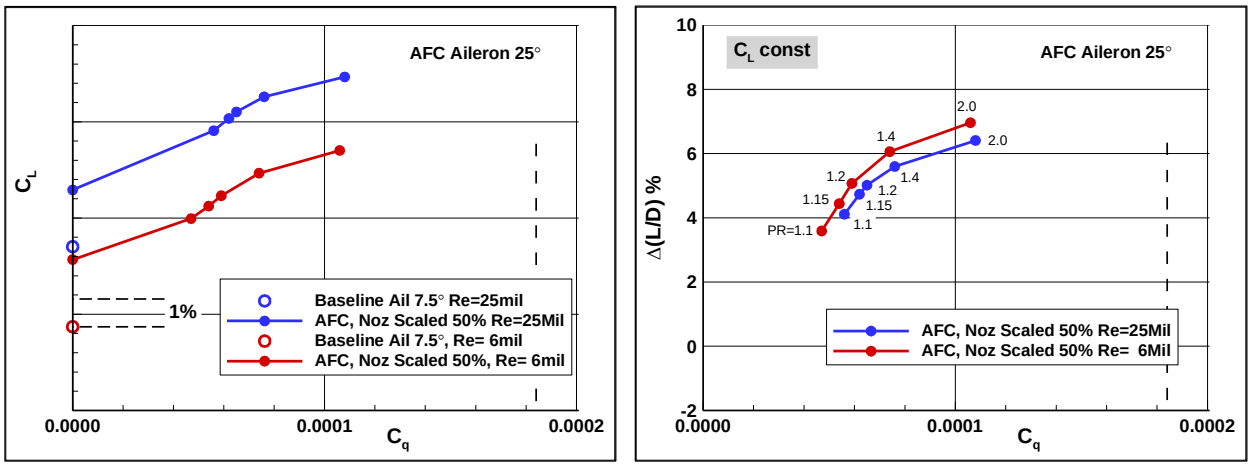

Fig. 44 Effects of Reynolds number on AFC at takeoff for Ail25.

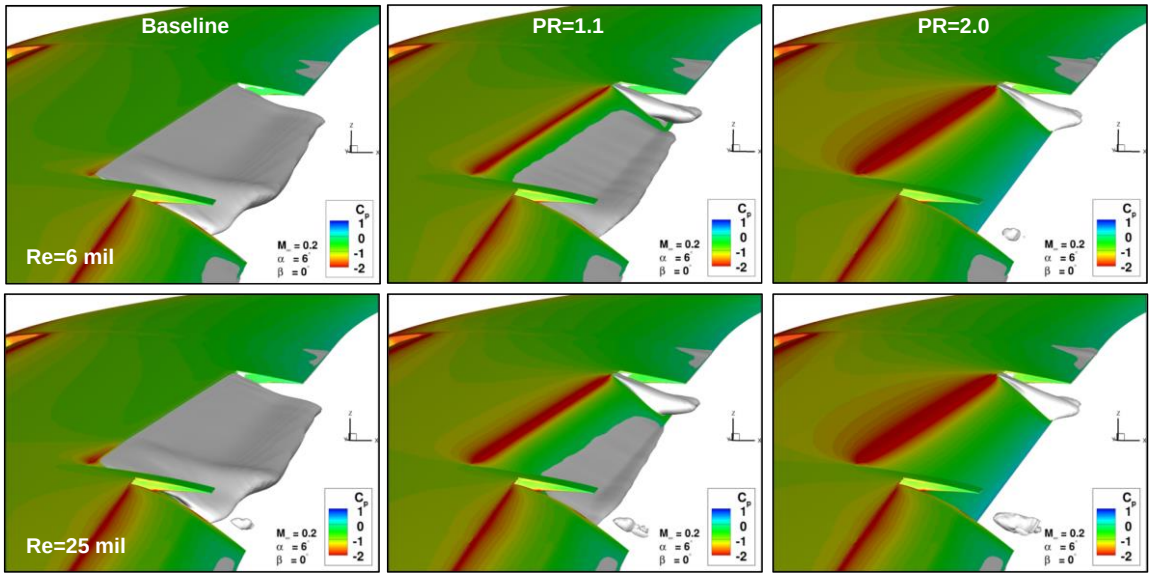

Fig. 45 Effects of Reynolds number on the flow fields with AFC at takeoff for Ail25, α=6°.

V. Conclusions

Flow control approaches for enhanced aerodynamic performance of ailerons were investigated numerically on a relevant commercial reference aircraft geometry. Steady blowing from elongated nozzles and discrete ducts were used in conjunction with deflected ailerons in order to reduce flow separation or outright remove it. Aileron deflections of up to 25° were considered. The increased lift and the reduction in drag results in improved L/D during takeoff, which is a major determinant of airplane performance. Improvements of more than 5% in L/D are achieved depending on the level of actuation applied. Even small pressure ratios achieve a significant effect on mitigating flow separation. The applied mass flows and supply pressure are within the feasible range of an APU. The flow control also provides increased C_{Lmax}. The AFC methods were designed for the least amount of actuation input in order to enable practical integration using onboard sources. The system integration study in the companion paper will help identify the most practical candidates. Changes in actuator size and distribution appear well governed by the momentum coefficient, which can be used to size the AFC configuration in order to provide the required momentum coefficient within the limitations of the available air sources. The findings of this study provide guidelines for a planned wind tunnel test for experimental confirmation of the AFC approaches. Additionally, the experimental data will be used to further refine the aircraft level integration and performance estimates, with the goal of enabling practical implementations into future airplanes.

Acknowledgements

This study was sponsored by NASA under Contract NNL16AA04B-80LARC20F0082. Dr. John C. Lin and Mrs. Latunia Melton were the NASA Langley Research Center Principal Investigators.

References

1. Hartwich, M.P., Camacho, P., El-Gohary, K., Gonzales, A.B., Lawson, E.L. and Shmilovich, A., "System-Level Trade Studies for Transonic Transports with Active Flow Control (AFC) Enhanced High-Lift Systems," AIAA 2017-0321, DOI: 10.2514/6.2017-0321
2. Shmilovich, A., Yadlin, Y., Dickey, D.E., Hartwich, M.P., & Khodadoust, A., "Development of an Active Flow Control Technique for an Airplane High-Lift Configuration," *AIAA SciTech Forum*, Grapevine, TX, Jan 9-13, 2017, DOI: 10.2514/6.2017-0322
3. Whalen, E.A, Shmilovich, A., Spoor, M., Tran, J., Vijgen, P., Lin, J.C., & Andino, M., "Flight Test of an Active Flow Control Enhanced Vertical Tail", *AIAA Journal*, Vol. 56, No. 9, 2018, DOI: 10.2514/1.J056959
4. Garner, P., Meredith, P., & Stoner, R., "Areas for future CFD development as illustrated by transport aircraft applications", *AIAA 10th Computational Fluid Dynamics Conference*, Honolulu, HI, June 24-26, 1991, DOI: 10.2514/6.1991-1527
5. Shmilovich, A. & Yadlin, Y., "Flow Control for Enhanced Airplane Takeoff Performance", *AIAA SciTech Forum*, Orlando, FL, Jan 6-10, 2020, DOI: 10.2514/6.2020-0784
6. Shmilovich, A., Yadlin, Y., Vijgen, P., & Woszidlo, R., "Applications of Flow Control to Wing High-Lift Leading Edge Devices on a Commercial Aircraft," *accepted for AIAA SciTech Forum*, National Harbor, MD, Jan 23-27, 2023
7. Vijgen, P., Ziebart, A., Shmilovich, A., & Woszidlo, R., "Conceptual Integration Studies of Localized Active Flow Control on the Wing of a Commercial Aircraft," *accepted for AIAA SciTech Forum*, National Harbor, MD, Jan 23-27, 2023
8. Woszidlo, R., Shmilovich, A., & Vijgen, P., "Low-Speed Performance Enhancement using Localized Active Flow Control – Program Overview and Summary", *NASA Technical Reports Server*, April, 2022, document ID: 20220006728
9. Shmilovich, A., Vijgen, P., & Woszidlo, R., "Low-Speed Performance Enhancement using Localized Active Flow Control – Localized Active Flow Control Simulations on a Reference Aircraft", *NASA Technical Reports Server*, April, 2022, document ID: 20220006731
10. Vijgen, P., Ziebart, A., Shmilovich, A., & Woszidlo, R., "Low-Speed Performance Enhancement using Localized Active Flow Control – Integration Study of Localized Active Flow Control on a Performance Reference Aircraft", *NASA Technical Reports Server*, April, 2022, document ID: 20220006733

11. Shmilovich, A., Stauffer, M., Woszidlo, R., Vijgen, P., "Low-Speed Performance Enhancement using Localized Active Flow Control – Simulations, Scaling and Design of Localized Active Flow Control on the Common Research Model", *NASA Technical Reports Server*, April, 2022, document ID: 20220006736
12. Buning, P.G., Chiu, I.T., Obayash, S., Rizk, Y.M., & Steger, J.L., "Numerical Simulation of the Integrated Space Shuttle Vehicle in Ascent", *15th AIAA Atmospheric Flight Mechanics Conference*, Minneapolis, MN, Aug 15-17, 1988, DOI: 10.2514/6.1988-4359
13. Shmilovich, A., & Vatsa, V., "Practical Computational Methods for Airplanes with Flow-Control Systems," *AIAA Journal*, Vol. 57, No 1, 2019, DOI: 10.2514/1.J056876
14. Shmilovich, A., "Unconventional Applications and New Approaches for Flow Control", in *Fundamentals of High Lift for Future Civil Aircraft, Notes on Numerical Fluid Mechanics and Multidisciplinary Design*, Springer book series, Vol. 145, Edited by Radespiel and Semaan, 2020, DOI: 10.1007/978-3-030-52429-6_1
15. Shmilovich, A., Yadlin, Y., & Whalen, E., "Computational Evaluation of Flow Control for Enhanced Control Authority of a Vertical Tail," *AIAA Journal*, Vol. 54, No 8, 2016, DOI: 10.2514/1.J054712
16. Shmilovich, A., Yadlin, Y., & Whalen, E., "Active Flow Control Computations: From a Single Actuator to a Complete Airplane," *AIAA Journal*, Vol. 56, No. 12, 2018, DOI: 10.2514/1.J056307
17. Shmilovich, A., & Yadlin, Y., "Flow Control for the Systematic Buildup of High Lift Systems," *AIAA Journal of Aircraft*, Vol. 45, No. 5, 2008, DOI: 10.2514/1.35327
18. Chakravarthy, S., "A Unified-Grid Finite Volume Formulation for Computational Fluid Dynamics," *International Journal for Numerical Methods in Fluids*, Vol. 31, No. 1, 1999, DOI: 10.1002/(SICI)1097-0363(19990915)31:1%3C309::AID-FLD971%3E3.0.CO;2-M